Characterization of On-Orbit GPS Transmit Antenna Patterns for Space Users

Jennifer E. Donaldson, Joel J. K. Parker, Michael C. Moreau, *Goddard Space Flight Center, NASA*

Dolan E. Highsmith, Philip Martzen, *The Aerospace Corporation*

Corresponding author:

Jennifer E. Donaldson
NASA Goddard Space Flight Center
M.S. 595.0
8800 Greenbelt Rd
Greenbelt, MD 20771
(301) 614-7079
<fax>
jennifer.e.donaldson@nasa.gov

Keywords: GPS spacecraft navigation, weak-signal GPS receivers, GPS space service volume

Characterization of On-Orbit GPS Transmit Antenna Patterns for Space Users

Jennifer E. Donaldson, Joel J. K. Parker, Michael C. Moreau, *Goddard Space Flight Center, NASA*

Dolan E. Highsmith, Philip Martzen, *The Aerospace Corporation*

Abstract

The GPS Antenna Characterization Experiment (GPS ACE) has made extensive observations of GPS L1 signals received at geosynchronous (GEO) altitude, with the objective of developing comprehensive models of the signal levels and signal performance in the GPS transmit antenna side lobes. The experiment was originally motivated by the fact that data on the characteristics and performance of the GPS signals available in GEO and other high Earth orbits was limited. The lack of knowledge of the power and accuracy of the side lobe signals on-orbit added risk to missions seeking to employ the side lobes to meet navigation requirements or improve performance. The GPS ACE Project filled that knowledge gap through a collaboration between The Aerospace Corporation and NASA Goddard Spaceflight Center to collect and analyze observations from GPS side lobe transmissions to a satellite at GEO using a highly-sensitive GPS receiver installed at a ground station. The GPS ACE architecture has been in place collecting observations of the GPS constellation with extreme sensitivity for several years. This sensitivity combined with around-the-clock, all-in-view processing enabled full azimuthal coverage of the GPS transmit gain patterns over time to angles beyond 90 degrees off-boresight. Results discussed in this paper include the reconstructed transmit gain patterns, with comparisons to available pre-flight gain measurements from the GPS vehicle contractors. For GPS blocks with extensive ground measurements, the GPS

ACE results show remarkable agreement with ground based measurements. For blocks without extensive ground measurements, the GPS ACE results provide the only existing assessments of the full transmit gain patterns. The paper also includes results of pseudorange deviation analysis to assess systematic errors associated with GPS side lobe signals.

1 Introduction

This manuscript describes an exhaustive dataset collected over a period of several years by the GPS Antenna Characterization Experiment (ACE) and the meticulous post-processing campaign to construct detailed maps of gain and pseudorange deviations for each of the satellites in the current GPS constellation. The antenna pattern maps resulting from this work provide verification of ground measurements of GPS satellite antenna gain patterns, and are expected to greatly facilitate the analysis of GPS performance for future Geosynchronous Orbit (GEO) or other High Earth Orbit (HEO) space applications.

There are a number of examples in recent years of operational space missions utilizing GPS measurements in GEO and HEO, and the demonstrated navigation performance for these missions has greatly exceeded pre-launch expectations in many cases [1, 2, 3]. These missions realize such exceptional performance for several reasons: transmitted GPS power levels exceed formal specifications of performance; receiver technology has evolved to reliably track very weak GPS signals; and transmissions from the GPS satellite antenna side lobes, which are completely excluded from performance specifications, contribute significantly to signal availability and improve the geometry of tracked satellites. As a result, most receiver performance simulation and testing for these applications has been conservative.

Space navigators have long sought to better understand the actual on-orbit performance of the GPS system available to HEO users, but publicly available data, particularly related to the performance of side lobe signals, has been limited. In 2006, NASA, U. S. Air Force (USAF), and Aerospace Corporation personnel worked together to document Space Service Volume requirements for GPS III, establishing a minimum specification for signal strength and availability of main-lobe GPS transmissions [4]. This formal expansion of the GPS performance regime to a *space service volume* (SSV) was a positive

development—this addressed the risk that many space missions already utilizing GPS in these orbital regimes were doing so without formal requirements governing future performance. Unfortunately, this specification defined conservative performance requirements based on the worst performing satellites in the GPS constellation at the time, without considering contributions from side lobe transmissions. As a result, the specified signal availability documented in the formal GPS III requirements vastly underestimates the number of signals demonstrated to be available on recent missions.

In 2015, Lockheed Martin publicly released measurements of Block IIR and IIR-M transmit antenna patterns collected during pre-launch testing [5]. This provided a detailed look at signal variations as a function of azimuth and elevation for all of the Lockheed-built IIR and IIR-M satellites. In spite of this excellent dataset, there is still no comparable publicly available dataset on the Block II/IIA/IIF satellites, or future GPS satellites. Moreover, questions still remained regarding how well the ground measurements matched actual on-orbit transmissions, and what measurement errors a user might experience when using side lobe signals.

The GPS Antenna Characterization Experiment began as a research collaboration between The Aerospace Corporation and NASA Goddard Space Flight Center (GSFC) to conduct a comprehensive characterization of the on-orbit GPS L1 transmit antennas. In this unique experimental set-up, GPS signals are received by a satellite in a GEO orbit and relayed to the GPS receiver and processing equipment located in the satellite ground station. In this manner, the GEO satellite serves as a *bent-pipe* relay, delivering the GPS signals to the user on the ground, not unlike the way many RF communications relay satellites work. Two GPS receivers are implemented in the ground station: a software version of the Goddard Navigator GPS receiver, with a sensitivity of approximately 22–25 dB-Hz [6]; and the Aerospace Mariposa GPS Receiver (MGPSR), which through the use of deeply-aiding tracking techniques is able to record GPS signals as low as 0 dB-Hz. The combination of the extreme weak signal sensitivity of the MGPSR and the operation of the experiment for multiple years has resulted in an exhaustive collection of GPS measurements spanning nearly every azimuth and elevation angle combination for each GPS satellite, enabling an in-depth analysis of the on-orbit performance of the GPS transmissions available to space

users. This manuscript provides a high-level overview of the experiment configuration and describes the comprehensive post-processing campaign, including link budget error models and techniques employed to identify and remove outliers in the dataset. Finally, the resulting antenna gain and pseudorange deviations results are presented.

2 Previous Work to Characterize GPS Signals in Space

Some of the earliest references regarding the use of GPS for GEO satellites are publications by Jorgensen in 1982 [7] and Wu et al. in 1992 [8]. Figure 1 illustrates the geometry associated with GPS signal transmissions available to users in HEO. Strong GPS signals emanating from greater than 13.8 degrees off-boresight pass by the limb of the Earth and may be received by satellites on the opposite side of the Earth, but many weaker signals from the side lobes may also be available. Also noted in this figure is the 23.5 degree limit of the SSV specification for L1 signals, which corresponds approximately with the null between the main lobe and the first side lobe of most GPS satellites. In 2001, Moreau's thesis [9, 10] presented a GPS receiver architecture for navigation in this regime, and around this time results from a number of early flight experiments and applications became available. This included Falcon Gold 1997 [11], Equator-S in 1998 [12], AMSAT OSCAR-40 in 2000 [13], and a paper by Kronman describing a bent-pipe GPS navigation system used in conjunction with a GEO satellite [14]. These early experiments, while generally successful, provided only a very limited amount of data on actual GPS signal levels. Nevertheless, there were sufficient data, particularly from the NASA-sponsored AMSAT OSCAR-40 experiment, to make it clear that significant variations existed in transmitted power levels between different blocks of GPS satellites. The AMSAT experiment also provided indications that some side lobes signals were significantly stronger than predicted from the limited data available at the time. These insights prompted NASA personnel who were evaluating the application of GPS to HEO missions to re-evaluate the applicable GPS performance requirements.

In this time frame, the official GPS specifications relating to signal strength and availability extended only to the Earth's limb. The main transmitting beam of the GPS satellite L1 antennas was typically assumed to measure a half-power angle of 21.3 degrees [15], but there was very little published information

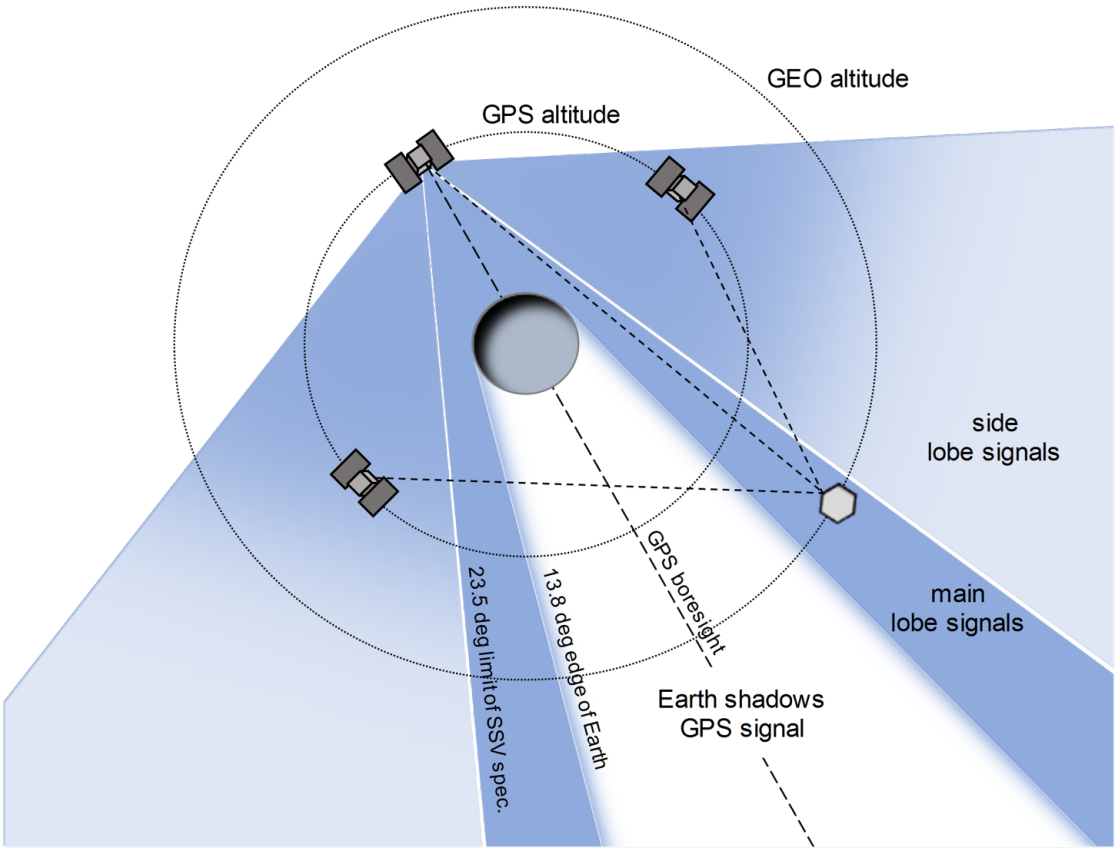

Figure 1: The geometry for reception of GPS signals in high Earth orbits.

regarding the GPS transmissions outside of a 14.3 degree half-angle, or possible variations in the shape of the GPS transmitter antennas, particularly in the side lobes. For many years, the only published data on the GPS L-band antenna pattern consisted of a paper by Czopek published in 1993 [16] that included four azimuth cuts of the relative gain from a Block II antenna. Data from the AMSAT experiment provided evidence that the main lobes of the Block IIR satellites were actually slightly narrower than the Block II/IIA patterns, and that at least some side lobe transmissions from Block IIR satellites were significantly stronger than what had been expected based on the Czopek data [13]. These observations were subsequently confirmed through data provided by Lockheed Martin, collected as part of the ground test program for the Block IIR and IIR-M antenna panels prior to launch. However, these data were not made available to the general user community until 2015 [5].

The insights gained through the AMSAT experiment demonstrated a need to better understand GPS

signals available to space users and to consider documenting formal requirements for this performance. In response, Bauer et al. proposed metrics for GPS signal performance requirements in two SSV regimes: medium altitudes from 3,000 km to 8,000 km, and high/geosynchronous altitudes from 8,000 km to 36,000 km [4]. More recently, GPS has been utilized by a wide number of operational HEO GPS applications [1, 2, 17, 18]. Each of these missions has demonstrated that through exploitation of transmissions from the side lobes of the GPS antenna pattern, the number of usable signals for navigation far exceeds what is predicted by the formal SSV requirements. NASA has continued to work with USAF to re-evaluate the GPS SSV requirements and consider whether revisions should be made to better reflect the performance currently realized by a number of civilian and military space applications of GPS [19]. However, in the time frame leading up to the acquisition of the GPS IIIF program, a consensus to adopt changes to the existing requirements was not reached.

Prior to the analysis of the GPS ACE data set, the best source of information on the GPS satellite gain patterns is the dataset on the Block IIR and IIR-M satellites described by Marquis [5]. A much more limited set of ground based antenna pattern measurements are available for the Block IIF satellites, but the side lobe measurements are only available for four azimuthal cuts through the antenna pattern, and the data are not publicly available. The European Space Agency published results from the GIOVE-A GPS experiment in 2013 [20], and a more exhaustive analysis of these results in 2017 [21]. The receiver on the GIOVE-A satellite performed up to 10 millisecond integrations and was able to record a large number of measurements of the stronger side lobe signals, providing limited insight into Block IIA and IIF antenna patterns for the first time.

3 GPS ACE Project Description

The GPS ACE collaboration between Aerospace and NASA GSFC began through respective independent research and development efforts, authorized though a NASA Space Act Agreement. The project began with significant receiver development efforts on both sides. Aerospace produced MGPSR, an ultra-weak signal tracking software defined radio receiver described in Section 3.2. NASA contributed two versions of its Navigator GPS Space Receiver platform [6]: a software defined radio version of the Navigator

receiver flight software, and a version of the same receiver algorithms implemented in a commercial off the shelf (COTS) field-programmable gate array (FPGA) development board. The Aerospace MGPSR and Navigator receivers are complementary—the MGPSR is a highly-aided, near-real-time receiver suitable for implementation as part of a navigation ground architecture, while the Navigator is an on-board, unaided receiver designed for autonomous, real-time navigation applications.

Once the receivers were built and tested, they were installed at a GEO satellite ground station and configured to track the GPS L1 signals received by the GEO satellite and relayed to the ground station in a bent-pipe architecture. The goal of the project was to track the GPS L1 transmitters over a period of time sufficient to produce a data set of GPS carrier-to-noise-density ratio (C/N_0) and pseudorange measurements spanning every GPS transmitter azimuth and elevation angle combination for each GPS satellite in orbit. Ultimately, this data set would be used to recreate the GPS transmit antenna gain patterns and generate pseudorange deviation assessments for all of the GPS satellites from Blocks IIA, IIR, IIR-M, and IIF.

3.1 GPS ACE Project Architecture

The GPS ACE system architecture is depicted in Figure 2. Beginning at the top left, the GPS vehicles transmit L1 C/A signals at 1575.42 MHz. These signals are received at the GEO spacecraft with a GPS patch antenna. A sample bandwidth centered around L1 is downconverted and transponded to the ground station on a telemetry channel dedicated to GPS, such that the GPS L1 spectrum is continuously available at the station where it is digitized and distributed on a local network. The autonomous GPS receivers process the digital data samples obtained from the network, and output GPS observation files containing pseudorange, carrier and carrier-to-noise ratio measurements.

Given the continuous availability of the transponded GPS L1 baseband at the ground station, the GPS ACE receivers produce daily observation files with a full 24 hours of tracking down to the sensitivity of the respective receivers: 22 dB-Hz for the NASA Navigator at 20 ms integrations and less than 0 dB-Hz for the Aerospace MGPSR at 30 s integrations. The extreme sensitivity of the MGPSR enables

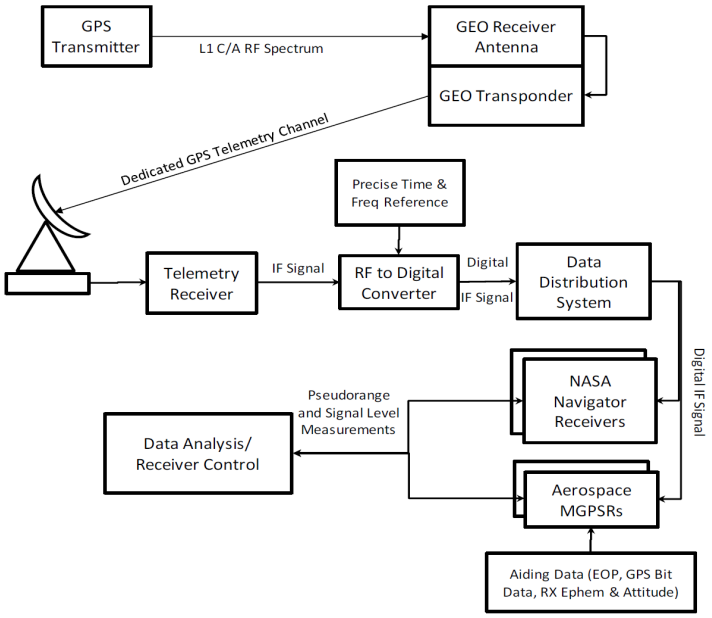

Figure 2: GPS ACE data collection architecture.

reconstruction of the GPS transmit gain patterns deep into the side lobes, to beyond 90 degrees off-boresight. The following subsections describe the MGPSR and Navigator GPS receivers in more detail.

3.2 Mariposa GPS Receiver (MGPSR)

The Mariposa GPS Receiver (MGPSR) is an Aerospace Corporation-developed ground-based software receiver that uses a highly aided, long integration batch processing algorithm. It was developed to operate in a non-real-time ground environment and process low signal-to-noise ratio (SNR) digital samples of GPS RF collected at orbital altitudes. Its roots derive from the data processing of the U. S. Air Force Academy-sponsored Falcon Gold experiment that was flown in November 1997 to measure GPS signals at high orbital altitudes [11]. The Falcon Gold data set, collected in a geosynchronous transfer orbit, contributed to the MGPSR design objectives and was used in work at the University of Colorado [22].

The current algorithm and design approach derive from orbit determination applications involving weak signal bent-pipe GPS in an aided post-processing mode. In this mode, the GPS base-band data is captured and queued for processing a short time later when the following aiding information is available:

a) GPS broadcast ephemeris and clock, b) approximate transponder ephemeris, and c) raw GPS subframe bit data. The subframe bit data is used for data wiping, while the transponder ephemeris and the GPS ephemeris and clock are used in the signal model construction. Together they enable long coherent integration.

The MGPSR batch processing algorithm does not use conventional signal tracking. After initial installation and periodically thereafter, the receiver correlator outputs are monitored, and then model path delays are manually adjusted to zero out average correlator offsets.

The following sections describe the signal model for the expected GPS signal, the long coherent integration method, and the generation of the C/N_0 measurements used in the reconstruction.

3.2.1 High Fidelity Signal Model

The MPGSR uses prior transponder ephemeris, GPS broadcast ephemeris and clock, along with a high fidelity signal model to generate replica samples of the GPS signal for use in the correlator described in the next section. The signal model fidelity is sufficient for a use in a 30-sec coherent synthetic complex ambiguity function (CAF). Under nominal tranponder conditions, the CAF peak offsets are much less than 1 Hz in frequency and 1 μs in time.

The GPS broadcast ephemeris and clock are obtained from externally supplied GPS sub-frame raw bit data. This data is decoded to obtain the clock and ephemeris message. In addition, the raw 50 bps bit data is included in the generated replica signal samples.

The model for the digitized signal can be described with Figure 3. In general, this signal originates from the GPS satellite, is received by the transponder, is down converted with an ideal mixer using a ground based local oscillator (LO) frequency, then is transmitted to the ground where it is digitized.

The light time diagram in Figure 3 provides a notional graphical solution for the signal propagation time between points in space. The notional range is on the y-axis and time is on the x-axis. The time line

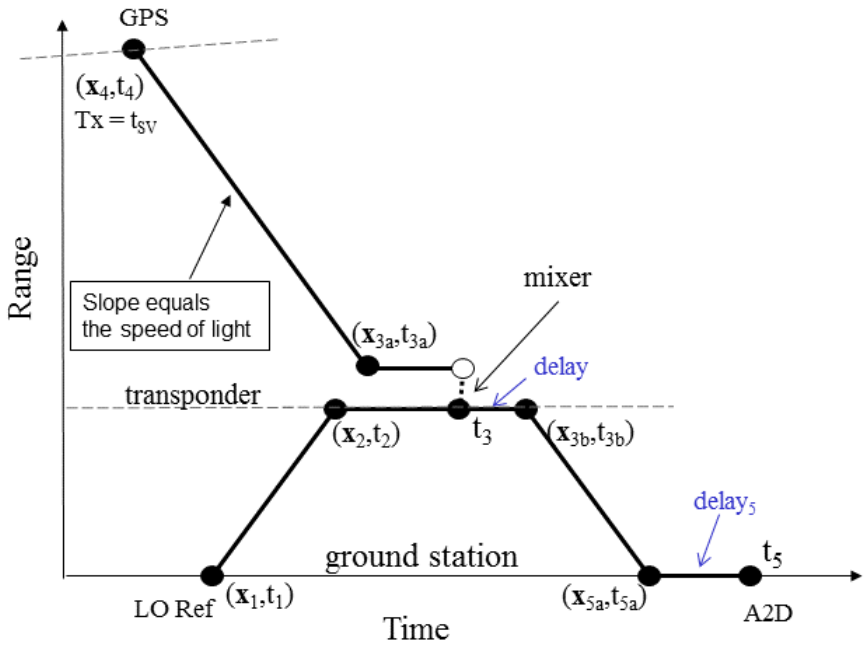

Figure 3: MGPSR Signal Model Light Time Diagram.

of an object lies along a nearly horizontal line, where the slope is the velocity. Light and radio signals travel at the speed of light between the time lines of objects. The light time diagram shows the earlier time of transmission of the signal digitized by the A2D converter at time t_5. This signal is a combination of a GPS signal and a local oscillator (LO) signal. The GPS signal was transmitted by the GPS space vehicle (SV) at time t_4 and arrived at the transponder at time t_{3a}. The LO signal was transmitted at time t_1 and arrived at the transponder at time t_2. The two signals were combined in the ideal mixer at time t_3 to form the down-converted GPS intermediate frequency (IF) signal. This signal left the transponder at time t_{3b} and arrived at the ground at time t_{5a}. After a ground delay it arrives at the analog-to-digital (A/D) converter at time t_5. Suppose the GPS signal transmitted at time t_4 contains the SV pseudorandom noise number (PRN) code phase time t_{sv}. This signal is digitized into a sample at time t_5. The GPSR effectively detects and reports the transmitted code phase time in the sample, reporting the raw pseudorange $t_5 - t_{sv}$, the sample time minus the code phase time. The carrier phase into the A2D converter at time t_5 is the GPS carrier phase at t_4 minus the LO phase at t_1.

In equation form, the signal model is expressed in terms of the propagation delay *retarded time* (see

Ref. [23] p. 185) as

$$t' = t - \frac{|\vec{x}(t) - \vec{x}'(t')|}{c} \tag{1}$$

where a signal emitted at position $\vec{x}'$ and earlier time t' is received at position $\vec{x}$ and time t. Let the signal captured by the A2D converter at time t_5 be

$$y(t_5) = A\, d(t_{sv})\, ca(t_{sv})\, e^{j\,2\,\pi\,(f_{GPSL1}\,t_{sv} - f_{LO}\,t_1 - f_S\,t_5)} + \eta \tag{2}$$

The constant A is the signal amplitude. The function $d(t_{sv})$ represents the subframe data, a 50 bps sequence of +1 and -1 values, evaluated at the GPS SV time, t_{sv}. The function $ca(t_{sv})$ represents the PRN CA spreading code, also evaluated at the GPS SV time. The GPS SV time, t_{sv}, is the SV PRN code phase time transmitted at time t_4 by the GPS vehicle. Let η represent the received noise. Let the received GPS emanations be downconverted in the transponder ideal mixer via a reference tone, f_{LO}, phase derived from the ground at time t_1 with a nominal difference frequency of 15.6 MHz, and then be band-pass filtered prior to transmission to the ground. The difference phase with a nominal frequency of 15.6 MHz arrives at the ground A/D converter at time t_5. The final term in the exponent is due to the band-pass sampling [24, sec 2.4] performed by the A/D converter. The sample rate is f_S with time reference t_5 and aliases the center frequency down to 3.1 MHz.

The equation for $y(t_5)$ does not explicity contain t_5, except for the band-pass sampling term. The times of transmission, t_4 and t_1, are related to t_5 via the *retarded time* Eq. 1. The equations are non-linear and can not be solved in closed form unless there is no motion. Instead, the solutions are tabulated as functions of t_5 and then converted to polynomials. Then, during correlation processing a sequence of replica samples corresponding to the signal samples is generated using equation 2 and the polynomials.

3.2.2 Long Coherent Integration Method

The extreme sensitivity of the MGPSR is enabled by the long coherent integration method described here. The method is dependent on the high fidelity signal model described in the previous section.

The carrier-to-noise ratio measurements used in the GPS transmit gain pattern reconstruction are derived

from the correlator output assuming the GPS signal has been found.

Due to model error, the replica will have small unknown delay and differential frequency offsets, which will cause the correlator output to be zero. Thus, the first task is to find the unknown offsets in time and in frequency.

As explained in [25], it is required to jointly estimate the time delay and the frequency difference in order to adequately obtain either. This is accomplished by computing the CAF shown in Eq. 3.

$$CAF(\tau, \delta f) = \sum_{k=0}^{n} y_k \, r_{k+i}^{*} \, e^{-j \, 2\pi \, k \, \delta \, f \Delta \, t} \tag{3}$$

In this expression, y_k and r_{k+i}^{*} represent the sequence of signal and replica samples, respectively; τ is the differential time delay; δf is the frequency offset; Δt is the sample interval; $i = \tau / \Delta t$ is the shift between the signal and replica sample index; and the summation is over the n samples included in the CAF. The τ and δf parameters are searched simultaneously for the $|CAF(\tau, \delta f)|$ peak. If a signal is present, a CAF correlation peak will be found at the time τ_p and Doppler δf_p offsets correponding to the offsets between the received signal and the replica.

The MGPSR correlator performs long coherent integration by coherently combining fast Fourier transform (FFT)-generated 1 ms complex correlations using methods similar to those described in references [26, 27]. For example, for 30 s coherent processing, a set of 30,000 1 ms complex correlations are computed and stored in a 2-D array. This 2-D array of 1-msec complex correlations is called a pre-CAF (PCAF) and is a function of the time t of each 1 ms complex FFT, and of the correlation time offset τ within each 1 ms FFT. Some sub-set of the 1 ms correlation output is stored in each row of the PCAF depending on the time search window. Let the PCAF function be $PCAF(t, \tau)$.

The 30 s CAF is generated by coherent sums of m 1 ms correlations with rotations to synthesize frequency offsets as shown in Eq. 4. The method is effective when the frequency offsets are much less than 1 kHz.

$$CAF(\tau, \delta f) = \sum_{k=0}^{m} PCAF(t_k, \tau) \, e^{-j \, 2\pi \, \delta f \, t_k} \tag{4}$$

The objective is to find the τ_p, δf_p corresponding to the largest value of $|CAF(\tau, \delta f)|$.

The CAF function, Eq. 4, can be quickly searched using FFT methods by taking FFTs of the PCAF data over t at fixed τ offsets within the search window. This results in evaluations of the CAF on a coarse grid with frequency step $\Delta f = 1/T$ and time step Δt, where T is the integration time. These evaluations can be quickly searched to find the largest CAF value in the grid.

Once the CAF grid peak is located, an interpolation is performed to refine the peak location and obtain the output parameters, including the CAF peak value and the C/N_0.

3.2.3 C/N_0 Estimation

The received carrier-to-noise ratio C/N_0 of the GPS signal used in the transmit antenna pattern reconstruction is derived from the correlator output as

$$C/N_0 = 10 \log_{10} \left(\frac{SNR_{out}}{T} \right) = 10 \log_{10} \left(\frac{(P-1)}{T} \right) \tag{5}$$

where P is the correlator power ratio given by

$$P = \frac{|CAF(\tau_p, \delta f_p)|^2}{n \, \sigma^2} \tag{6}$$

T is the integration time in seconds, σ^2 is the sample variance, and n is the number of samples in the CAF. When no signal is present, the expected value for P is $P = 1$, or $SNR_{out} = 0$. The sample variance is computed as

$$\sigma^2 = \frac{1}{n} \sum (I^2 + Q^2) \tag{7}$$

where I are the in-phase samples, and Q are the quadrature samples, which is essentially a measurement of the wide-band noise power.

3.3 Navigator GPS Receiver

The NASA GSFC-developed Navigator GPS receiver is an L1 C/A, fast-acquisition, weak-signal-tracking spaceborne GPS receiver for high-altitude applications. It employs a FFT-based acquisition algorithm adapted from [26] and described in detail in [6]. This method allows the receiver to acquire weak GPS signals as low as 25 dB-Hz in real-time with no *a priori* information to aid the receiver. Additionally, the receiver uses a 20 ms long coherent integration to track weak signals as low as 22 dB-Hz.

At the time that GSFC began development of the Navigator in the early 2000s, there existed few commercially available GPS receivers capable of operating reliably above low-Earth orbit. GSFC had previously developed a GPS receiver called PiVoT based on a commercially available GPS chipset development kit. PiVoT incorporated customized software modifications that supported its use in HEO mission scenarios, and the receiver was used extensively in hardware in-the-loop testing and technology development activities. The PiVoT hardware did not support a path to flight qualification, which led to the development of Navigator as a new space-flight qualified HEO receiver. The first flight of the Navigator receiver was in 2009 as a technology demonstration on the Space Shuttle as part of the Hubble Space Telescope Servicing Mission 4 (HSM-4). It was first used operationally on NASA's Global Precipitation Measurement (GPM) mission in LEO, and subsequently Navigator was used for the on-board navigation system on the NASA Magnetospheric Multiscale (MMS) mission. The MMS mission features four spacecraft in highly elliptical orbits, and the Navigator receiver has demonstrated robust GPS performance at ranges from the Earth reaching nearly half way to the Moon [3]. The Navigator fast acquisition algorithms have been incorporated into the GPS receiver on the NASA Orion Crew Vehicle, and the design has been licensed to several commercial vendors of GPS receivers.

For the GPS ACE project, GSFC delivered two versions of the Navigator receiver, a software defined radio version of Navigator that runs in real-time on a Linux desktop computer and a re-programmable FPGA version of the receiver that runs on a COTS FPGA development board. The Navigator receiver was primarily used for real-time orbit determination experiments, which are not discussed in this paper, and for verification of the MGPSR measurements. The MGPSR was used for the antenna pattern

reconstruction because of the lower C/N_0 sensitivity.

4 Antenna Pattern Reconstruction

The GPS ACE measurements from the MGPSR are processed to reconstruct transmit antenna patterns for all observed GPS spacecraft. The objective is to precisely map individual received power measurements and other observed signal characteristics back to the corresponding azimuth and elevation angle of the GPS transmitter, such that GPS signal characteristics may be documented on a per-satellite basis. Due to the geometry between the 24 hour GEO orbits and the 12 hour GPS orbits, as well as the yaw of the GPS spacecraft, the transmit patterns slowly fill in over time. If there were no gaps in tracking, the patterns would be completely filled in with measurements after approximately six months. Figure 4 shows how the patterns fill in over time.

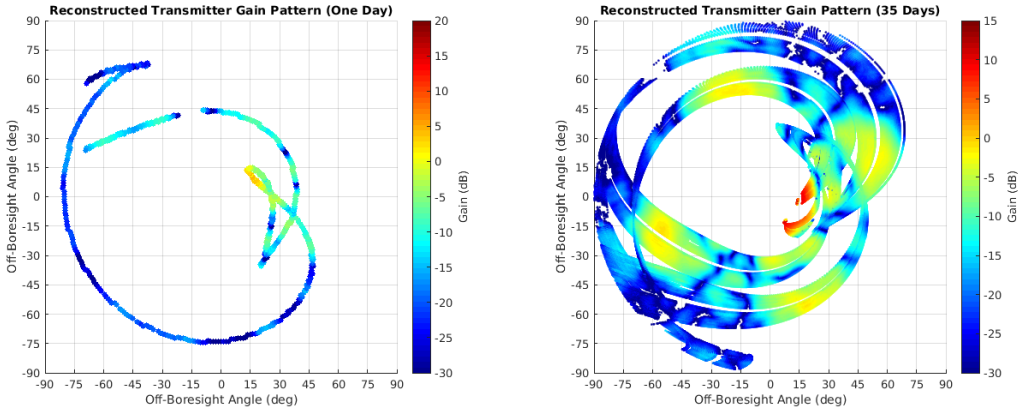

(a) (b)

Figure 4: Example of how the data collected by the MGPSR receiver slowly fills in the transmit antenna pattern over time. The perspective is from the GPS transmit antenna frame showing the path of the receiving spacecraft over time. Plot (a) shows one day of data collection, and Plot (b) shows 35 days of data collection.

Approximately two years of MGPSR measurements (non-continuous) were aggregated for post-processing and reconstruction of antenna gain and pseudorange deviations. Care was taken to exclude periods of time during which variations in the transmitted power levels from the GPS satellites were possible, such

as during the L1 C/A power testing activities announced on January 25, 2017 [28]. A sample of just one day of MGPSR 30 s observations from a GEO spacecraft is shown in Figure 5, which illustrates the extent of received signal levels and GPS off-boresight angles available in a single day of data.

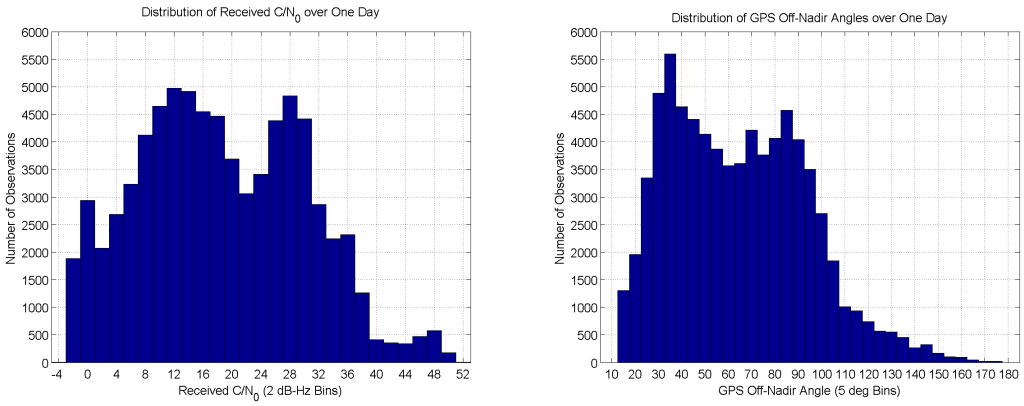

(a) (b)

Figure 5: Histograms of the number of MGPSR observations taken over one day from a GEO spacecraft. Plot (a) shows the distribution of observations with respect to received carrier-to-noise ratio (C/N_0) in 2 dB-Hz bins. Plot (b) shows the distribution with respect to GPS off-nadir or off-boresight angle in 5 degree bins.

The primary external tool used in the MGPSR data processing is the Orbit Determination Toolbox (ODTBX), an open source, MATLAB-based, orbit determination analysis tool developed at NASA GSFC [29]. ODTBX provides a variety of measurement simulation, estimation, and data visualization capabilities useful for early-phase mission analysis, including GPS pseudorange measurement models and a suite of GPS data analysis functions. The GPS models provide the ability to model physical parameters of the transmitters and receiver, including relative geometry and antenna patterns, perform link budget analyses to estimate either transmit or received power, and a full suite of plotting and visualization routines. These latter capabilities were the basis of much of the geometric and link budget analysis performed on the GPS ACE data.

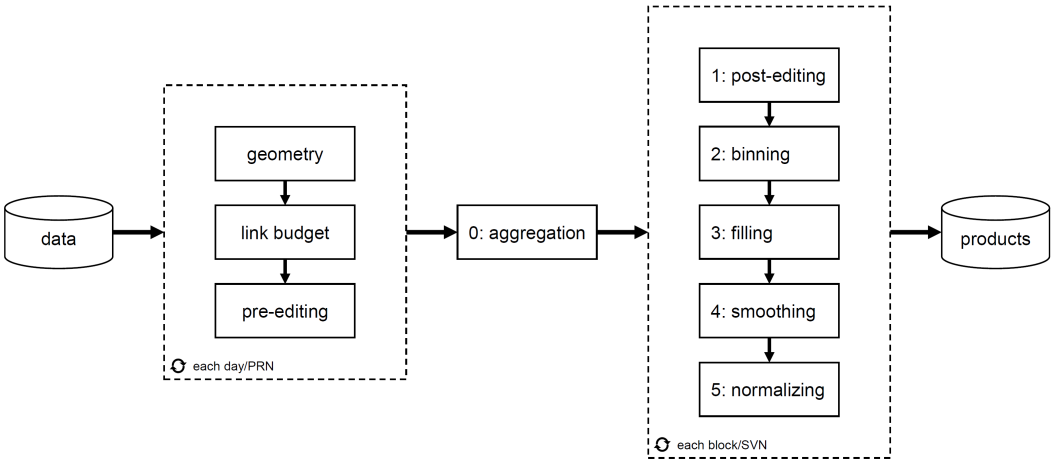

Figure 6: Gain pattern reconstruction process. Post-processing data levels (0–5) are indicated on each post-processing step.

4.1 Reconstruction Approach and Tools

The antenna gain pattern reconstruction process, shown in Figure 6, consists of two primary components: 1) an algorithm that uses the ODTBX software to reconstruct transmit gain from MGPSR receiver measurements and 2) a post-processing workflow that reconstructs a set of full patterns from a long-term batch of reconstructed measurements. Each of these major components, in turn, consists of the discrete steps described in this section.

The gain reconstruction process operates on C/N_0 measurements produced by the MGPSR receiver and uses ancillary data to resolve the receive/transmit geometry at each epoch, performs a link budget calculation to derive the GPS-transmitted gain value, and performs a number of quality checks at the measurement level. The MGPSR measurements are logged daily at 30 s intervals for each visible satellite. The reconstruction algorithm operates on each measurement for a single PRN on a single day, resulting in transmit azimuth and elevation angles along with calculated transmit gain for each C/N_0 measurement. The individual processes in this component are:

1. **Geometric modeling** captures the problem geometry and calculates GPS transmit antenna-relative azimuth and elevation angles for each measurement,

2. **Link budget modeling** reconstructs the transmit antenna gain value from a received C/N_0 measurement, and
3. **Pre-editing** uses problem knowledge to detect and remove outlier measurements.

To process multiple dates and PRNs, an automated batch-processing system was developed to generate results across the full set of available data. A post-processing workflow was established to aggregate the generated data and produce the final set of products, primarily antenna gain patterns for each on-orbit GPS SV and averaged patterns for each GPS block. The post-processing is divided into distinct processes:

0. **Aggregation** collects PRN-specific data into SV-specific and block-average datasets,
1. **Post-editing** performs outlier detection and removal at the pattern level,
2. **Binning** transforms spatially scattered measurements into a regular azimuth/elevation grid,
3. **Filling** uses interpolation to fill isolated missing bins,
4. **Smoothing** reduces noise in the final patterns, and
5. **Normalization** calibrates the final patterns against known independent sources such as ground-measured data.

Each of these processes is discussed in detail in the following sections.

4.2 Geometric Modeling

The physical, geometric modeling of the GPS signal path involves calculating the angle of transmission from the perspective of the GPS transmit antenna, which results in a calculated transmit antenna azimuth and elevation angle associated with each measurement. Numerous data sources are needed for this process, including receiver and transmitter ephemeris, attitude, and antenna characteristics; general parameters such as leap seconds; and the MGPSR measurements themselves.

The MGPSR measurement data is available in two-hour batches for each individual PRN, at a 30 s timestep. The available data consist of over thirty distinct parameters as output by MGPSR, but the

reconstruction process uses four primary ones: epoch, PRN, C/N_0, and pseudorange. This data is validated at the time of ingest by removing duplicated data values, and again during the measurement editing process. This 30 s timestep forms the fundamental timestep of the reconstruction process.

Several important details must be considered when mapping GPS ACE measurements back to the originating GPS satellite and transmit antenna geometry: GPS PRN to SVN mappings, SV block specific attitude models, and GPS constellation ephemeris. GPS transmit antenna designs have changed with each block, and in the case of Block IIR, even within a single block. Therefore, it is necessary to perform antenna pattern reconstruction relative to the physical GPS satellite vehicle number (SVN), rather than a given PRN spreading code, which may be reassigned. Because the MGPSR measurements are associated with the PRN, PRN-to-SVN mapping is done using a compiled history of PRN to SVN assignments. There are several sources for this data, including public files published by Analytical Graphics, Inc. (AGI) and the International GNSS Service (IGS). For this effort, an internal mapping dataset available within NASA and the USAF was utilized for convenience and validated against the public data to ensure agreement.

Each SVN was then mapped to a block type using publicly-available data. The block assignments used for this analysis differ from other sources because of the fact that four Block IIR satellites were configured with modernized antenna panels identical to those used on Block IIR-M vehicles. These were considered as part of Block IIR-M for the purposes of this analysis. Table 1 shows the SVN-block mapping used in this analysis, where the IIR satellites with modernized panels are indicated in bold.

ODTBX computed the GPS constellation ephemeris from publicly-available GPS YUMA almanac data. Employing the almanac published on the day of a particular batch of MGPSR observations put the measurement epoch near the center of the almanac validity period. Standard algorithms were used to calculate GPS vehicle position at a given epoch from the almanac. Some consideration was given to using broadcast ephemeris data or post-processed ephemeris data available from external sources, but the error introduced via use of almanac data was considered negligible, as described in Section 6.3. By comparing one day of YUMA propagated almanac data with National Geospatial-Intelligence Agency

Table 1: GPS SVN/block mapping. Bold font indicates Block IIR satellites with the modernized antenna panel, processed as IIR-M SVNs.

Block	**Tracked SVNs**
IIA	23, 26, 33–35, 38–40
IIR	41, 43–46, 51, 54, 56
IIR-M	**47**, 48, 50, 52, 53, 55, 57, 58, **59–61**
IIF	62–73

(NGA) precise SP3-format ephemerides for all PRNs, the maximum difference was found to be less than 4.2 km, less than 4% of the magnitude necessary to cause a threshold error of 0.5 degree or 0.1 dB in the resulting pattern.

For the transmitter attitude, the Bar-Sever model was implemented as described in [30]. This yaw model applies directly for the Boeing Block IIA and IIF satellites, in which the nominal attitude of the GPS satellites points the boresight of the GPS antenna at the center of the Earth and yaws about this axis in order to keep the solar panels perpendicular to the direction of the Sun. The nominal yaw angle is the angle of rotation about the $+Z$ body-fixed axis (nadir) from the velocity direction of the vehicle to the $+X$ body-fixed axis that ensures the $+X$ axis of the vehicle is pointing towards the Sun. The nominal yaw for the Lockheed Martin Block IIR and IIR-M satellites is oriented differently with the $-X$ axis pointed towards the Sun. Figure 7 shows this geometry for the yaw angle calculation for the various satellite blocks. The GPS satellites do not follow this nominal attitude behavior during a period of eclipse or when the nominal yaw rate would be too high at orbit noon (the *noon turn*) when the angle β between the Sun and the orbit plane is small. Because the behavior of the GPS satellites is not well defined during these periods, data during the low β angle and eclipse periods are not included in the antenna pattern reconstruction process. For the purposes of calculating the windows for which data was discarded based on attitude, the low β angle was set to $\beta < 5$ degrees and the eclipse was defined by the time periods when the angle between the satellite and the Sun was smaller than the extent of the Earth

penumbra.

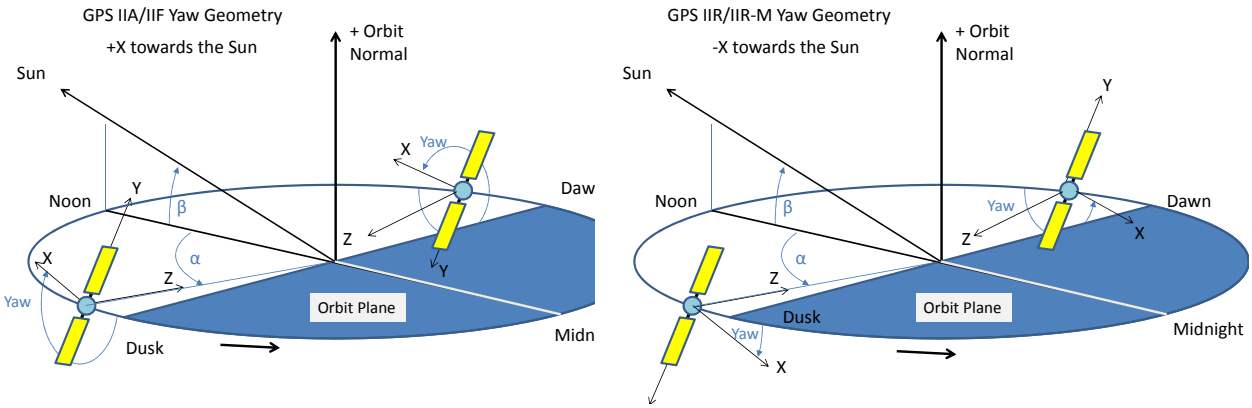

(a) (b)

Figure 7: Geometry of the GPS transmitter yaw model for Block IIA and IIF (a) and Block IIR and IIR-M (b). The yaw angle is defined as the rotation about the nadir pointed $+Z$ body-fixed axis from the velocity vector direction in the orbital plane to the $+X$ body-fixed axis.

For the receiving spacecraft, orbit position is available via ephemerides provided at a 5 min timestep in the Earth-centered, Earth-fixed frame. This data is first checked for validity and consistency, then is converted to the Earth-centered internal (J2000) frame and interpolated to the measurement times using divided difference Hermite interpolation. The Fifth Fundamental Catalog (FK5) reduction from Earth-fixed to inertial frames was performed using the IAU1980 nutation and precession model, and with a fixed polar motion model. Validity checks include expected timespan, expected orbit parameters, data discontinuities, invalid values, and large-scale visual spot-checks. All potential violations were logged as part of the automation process, investigated, and resolved via acceptance or exclusion of the data.

The receiving spacecraft attitude is provided via a variable-step Euler angle ephemeris at approximately 5 min intervals. The provided angles relative to the body frame are converted to quaternion form, where the angles are *unwrapped* to resolve sign discontinuities, and interpolated to the spacecraft ephemeris times via spherical linear (*slerp*) interpolation. The resulting body-frame attitude is then rotated through a series of documented, fixed rotations to the inertial frame and interpolated again by the same method to the measurement times. The resulting rotation is used to determine receiver antenna pointing and

yaw rotation about the boresight. Like the orbit ephemeris, the attitude is verified for validity and consistency by testing against expected timespans, expected pointing constraints, data discontinuities, invalid values and malformed attitude representations, and via visual spot-checks.

4.3 Link Budget

The effective isotropic radiated power (EIRP) of the GPS satellites cannot be directly measured with the GPS ACE data. Rather, it can only be inferred through carrier to noise density C/N_0 measurements, which include inherent modeling assumptions regarding system noise and other factors in the link budget. With knowledge of the received power R_p, the receiver antenna gain A_r, space-loss attenuation A_d, and the transmit power of the GPS satellite P_{sv}, the gain at the transmit antenna A_t can be found. However, because the true transmit power of the GPS satellites is unknown and because there is modeling uncertainty in other aspects of the link budget, this method cannot fully separate the transmit power and the gain from the EIRP. For this reason, a nominal transmit power value was chosen for each block of GPS satellites as specified in Table 2. These transmit values meet the minimum required GPS power levels at the edge of the Earth and account for estimated excess power above spec based on receiver tracking data and knowledge of the main lobe patterns.

Table 2: Constant link budget parameters assumed in the antenna gain pattern reconstruction.

Link Parameter	**Symbol**	**Value**	**Units**
Other Losses	$A_s + L_r$	-1.31	dB
Noise Temperature	T_s	175.84	K
Block IIA TX Power	P_{sv}	14.90	dBW
Block IIR TX Power	P_{sv}	15.00	dBW
Block IIR-M TX Power	P_{sv}	14.30	dBW
Block IIF TX Power	P_{sv}	14.30	dBW

The final reconstructed antenna gain patterns from the GPS ACE measurements are normalized with respect to the ground measured data available for each of the GPS blocks. A more detailed discussion

of the normalization method is presented in 4.8.

The fundamental measurement used for the antenna pattern reconstruction is the GPS receiver's estimated carrier-to-noise density ratio, C/N_0. In order to calculate the received power R_p, the noise of the system must be calculated. The effective antenna noise temperature is found by considering the thermal radiation from the Earth and the cosmic background. In general, the antenna noise temperature T_a is given by:

$$T_a = \frac{1}{4\pi} \int_{4\pi} G(\theta, \phi)\, T(\theta, \phi)\, \mathrm{d}\Omega \tag{8}$$

where $G(\theta, \phi)$ is the antenna gain and $T(\theta, \phi)$ is the noise temperature as functions of the antenna azimuth angle θ and elevation angle ϕ. When integrating the temperature over the unit sphere, the Earth temperature was assumed to be 290 K, and the cosmic background radiation was assumed to be 29 K at the GPS frequencies [31]. The receive antenna gain pattern was modeled as a second order polynomial which is uniform in azimuth. The thermal noise contributions from the Sun and Moon, when they were in the field of view, were transient and in the average, only changed the average antenna noise temperature by less than 1 K, so therefore, were not used.

The noise temperature of the front-end antenna electronics T_g, which include filters and low noise amplifier (LNA), can be found via the *Friis Formula* [32], assuming a fixed spacecraft temperature of 290 K and a fixed noise figure, NF_l, as:

$$T_g = 290\,(10^{\frac{NF_l}{10}} - 1) \tag{9}$$

It is also assumed that the LNA has a fixed gain, G (dB), and that there is a fixed cable loss, L (dB), between the front-end antenna electronics and the downconverter. The downconverter noise temperature T_d is a function of the noise figure of the downconverter, NF_d (dB), and the total linear gain before the downconverter, $g = 10^{(G+L)/10}$:

$$T_d = 290 \left(\frac{10^{\frac{NF_d}{10}} - 1}{g} \right) \tag{10}$$

Finally, the system noise temperature T_s is simply:

$$T_s = T_a + T_g + T_d \tag{11}$$

Other losses accounted for include the receive antenna polarization loss (before the LNA), A_s, and receiver loss, L_r, which includes the increase in the noise floor due to the presence of multiple GPS signals in the L1 band and the analog-to-digital conversion loss on the ground.

Because the GPS L1 spectrum is modulated onto a carrier on-board the spacecraft and then demodulated once received on the ground, the gain and noise figure of the space to ground link does not have an impact on the calulation of the GPS carrier-to-noise ratio. Essentially, the system noise for the L1 signals are *set* at the output of the mixer on-board the spacecraft.

The GPS signal carrier power at the receiving spacecraft just before the antenna is a function of the noise temperature of the receiver $N_0 = 10 \log_{10}(kT_s)$, where k is Boltzmann's constant, the measured carrier-to-noise density ratio C/N_0, the receiver antenna gain A_r, and the contributions from other losses, A_s and L_r. This relationship is shown in Eq. 12 where the losses are negative numbers (A_s, L_r, N_0) and the gains are positive numbers:

$$R_p = C/N_0 + N_0 - A_r + L_r + A_s \tag{12}$$

The GPS signal carrier power at the receiving spacecraft just before the antenna can also be determined from the transmitter antenna gain A_t, the transmitter output signal power P_{sv} (dBW), and the space-loss A_d (dB), which is a function of the distance between the transmitter and receiver and the link frequency L1:

$$R_p = A_t + P_{sv} + A_d \tag{13}$$

Since in this case, the transmit antenna gain is an unknown, the received power at the antenna calculated from the measured C/N_0 in Eq. 12 can be used to determine the transmitter gain by solving for A_t in Eq. 13 as shown in Eq. 14:

$$A_t(\theta, \phi) = C/N_0 + N_0 - A_r + L_r + A_s - A_t - P_{sv} \tag{14}$$

A summary of the link budget parameters is presented in Table 2 and a more detailed look at the variation in the link budget parameters is presented in Section 6.2.

4.4 Editing and Aggregation

Before the data is aggregated for each GPS satellite, various data editing routines were applied to remove any erroneous data. The first edit check is for the GPS spacecraft yaw attitude. All the data during noon turns and eclipse periods is removed because the behavior of the spacecraft is not well defined during those time periods. There are also periods of time in which the ground system configuration changed over the course of the multi-year data collection, which introduces intervals in which some of the MGPSR data is corrupted. To be conservative, all data recorded in the vicinity of configuration change periods was discarded. Finally, detailed analysis highlighted other periods of time when the MGPSR reported anomalous C/N_0 measurements attributed to anomalies with the receiver solution, or in some cases unexpected behavior of the GPS satellites. More details on these data editing methods and their verification is provided in Section 6.1.

The block-average patterns are generated by aggregating all measurements from SVNs within the block, prior to executing the post-processing steps. Table 3 summarizes the total number of measurements by block. Figure 8 shows the number of measurements per GPS SVN. SVNs 69–73 were the Block IIF satellites most recently added to the GPS constellation and, as such, were not available for GPS ACE

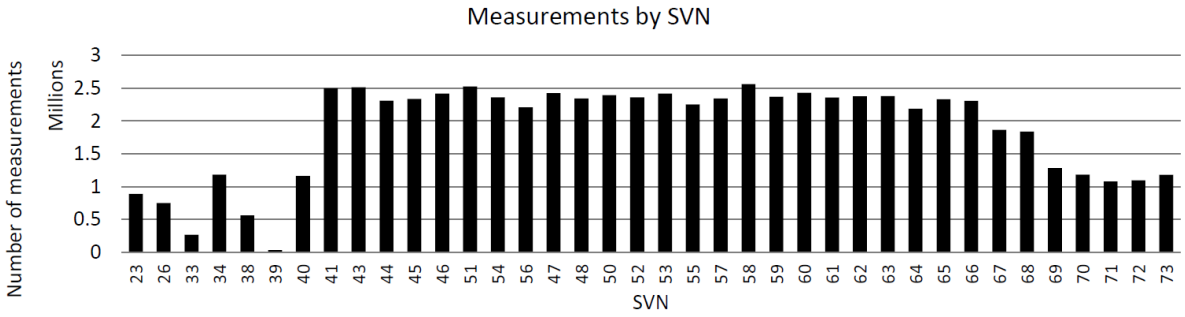

Figure 8: Quantity of measurements in dataset by GPS SVN. There are fewer measurements in the tails because the data set spans the period where Block IIA vehicles were being retired and Block IIF vehicles were being added.

data collection as long as some of the earlier satellites.

Table 3: Total number of measurements processed in each block. The IIR-M category includes IIR SVNs with the modernized antenna panel.

Block	**Total Measurements**
IIA	04.8M
IIR	19.1M
IIR-M	26.3M
IIF	21.1M

To generate a usable set of antenna patterns, a number of post-processing steps are implemented, as discussed in the following sections. As shown Figure 6, these steps are executed on each pattern individually.

Some remaining outliers become apparent after measurements are mapped to the transmit antenna coordinate frame. The pattern is processed in uniform bins of 1 degree in azimuth and elevation angle. A sigma (σ) value and mean is calculated for each bin, and all measurements outside of 3σ from the mean are removed. This process is repeated in two passes, with the statistics recalculated after the first pass. This editing step results in approximately 1% of measurements removed among the block-aggregated data.

4.5 Binning

The binning process interpolates scattered gain data onto a uniform azimuth/elevation grid for use as an input to mission analyses. There are many possible techniques that could be used for this process, with variables including the size of grid (the *bins*), the method for reducing the data within a bin, and the method for placement of the reduced bin value. In this case, the patterns were divided into a 1 degree azimuth/elevation grid with bin centers at integer values from 16 to 90 degree off boresight across all azimuths, for a total of 27,000 bins. Data coordinate azimuth/elevation values were rounded for bin assignment, such that a value located at 18.3 degree elevation and 54.5 degree azimuth would be placed in the 18 degree/55 degree bin. Within each bin, the mean is calculated of all gain values present in the bin, and the value is placed at the bin center. Some consideration was given to other values of bin size (0.25 degree–2 degree) and reduction methods (mean, interpolation, nearest-neighbor, etc.). The adopted methods were chosen as the best combination of data volume, feature resolution, and simplicity.

4.6 Filling

Even with the measurement quantities shown in Figure 8, many SVN-specific patterns remain incomplete, with gaps in the grid varying from a few scattered empty bins, to large-scale incomplete features (particularly for some of the Block IIA SVs). Therefore, a step was implemented, when feasible, to interpolate into the gaps using data from the surrounding bins to form a *filled* pattern.

Recognizing that only small gaps will be recoverable, a threshold of 90% was established for pattern completeness—if the percentage of filled bins in a given pattern was less than this threshold, gap-filling was not attempted. Once the threshold was met, interpolation was performed using a linear radial basis function interpolator as implemented by the SciPy Python package [33].

Figure 9 shows the SVN 62 pattern both before and after application of the gap-filling step.

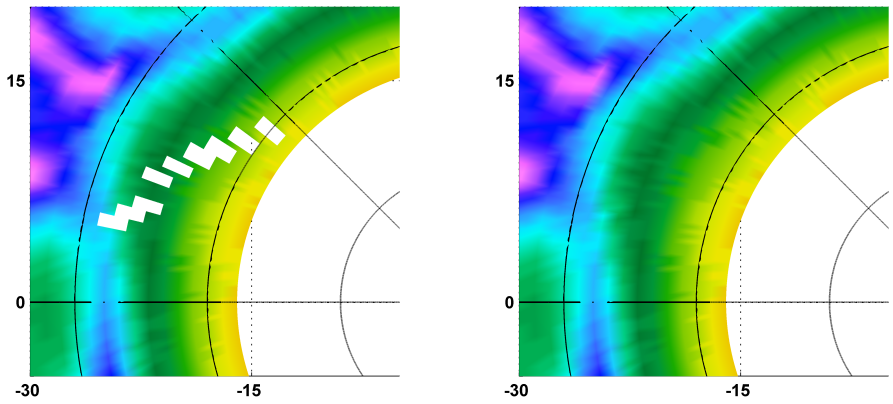

(a) (b)

Figure 9: Example of linear radial basis function interpolation used to fill gaps in SVN 62 pattern. Image (a) features a series of 1x1 degree gaps due to missing measurements in those bins. Image (b) shows the interpolated pattern.

4.7 Smoothing

The binned and filled data is an average of a large number of individual points in each individual bin, which does not create a smooth antenna profile, especially where the data was sparse or missing. It was also found that the data in the main lobe is noisier than the rest of the antenna pattern. This is assumed to be attributed primarily to the steep slope of the gain pattern in this region in conjunction with the long (30 s) integration period of the MGPSR. A secondary contributor to noisier main lobe signals could be perturbations induced as main lobe signals pass closely by the limb of the Earth. However, only GPS signals with a transmit off-boresight angle of 16 degree or greater, corresponding to a height of ray-path (HORP) altitude of approximately 1,200 km, were included in post-processing. To mitigate bin-to-bin measurement noise, a two-dimensional Gaussian lowpass filter was applied to the individual patterns after the filling step. The end result is a smoother pattern that can be used to compare against ground measured data. Figure 10 shows the azimuthal variation at 18 degree off-boresight in a block IIR antenna pattern and the output of the smoothing process.

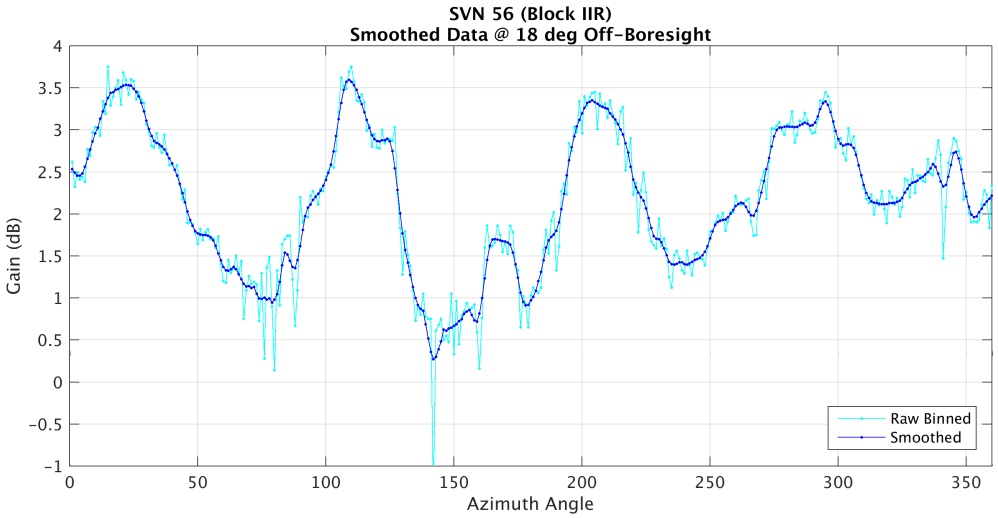

Figure 10: Example data from a block IIR (SV 56) satellite. The binned data is smoothed with a Gaussian lowpass filter.

4.8 Normalizing

As mentioned previously, the true transmit power of the GPS satellites is not publicly available information; therefore, there exists an unknown parameter in the link budget which makes it difficult to determine the absolute isotropic gain for the reconstructed antenna patterns. However, the L1 transmit directivity and gain patterns for each individual Block IIR and IIR-M satellite are publicly available and can serve as an anchor point for the reconstructed patterns. Additionally, the Aerospace and NASA GPS ACE team members have access to Block IIF gain patterns of the main lobe response at L1 that to-date have not been released to the public. The final step in the antenna pattern reconstruction process uses these data sets to *normalize* the gain patterns to these reference data sets, thereby producing a final product that should closely represent the absolute gain of the GPS antenna panels, separate from the transmit power.

The normalization method involves taking multiple elevation cuts from 16 to 23 degree off-boresight in the main lobe at 1 degree steps in azimuth and then finding the least squares best fit of the smoothed data to the ground measured data. The average of the best fit offsets is then calculated which results in one absolute scaling parameter per SV. A summary of the mean offset per block, which represents a

combination of the difference between the approximate transmit power and the true power and the other uncertainties in the link budget, is presented in Table 4. These offsets are then applied globally to the per SV patterns to produce the final reconstructed antenna gain products. For the Block IIA patterns, measured antenna pattern data was not available to reference, so the IIF data was used in its place due to their similarities. Additionally, to create the block-average patterns, the final individual normalized patterns were averaged together bin-by-bin to produce the final products.

Table 4: Mean global offsets per block used to normalize the final reconstructed antenna patterns. Block IIA SVs 33, 35, and 39 are not included in this list because they were removed from the constellation before enough data could be recorded.

Block	**SVNs**	**Mean Global Offset (dB)**
IIA	23, 26, 34, 38, 40	5.6
IIR	41, 43–46, 51, 54, 56	5.3
IIR-M	47, 48, 50, 52, 53, 55, 57–61	4.0
IIF	62–73	4.6

5 Results

5.1 Reconstructed Transmit Antenna Patterns

This section presents an overview of the final products generated from the post-processing of the GPS ACE measurements. Full results have been released as supplementary data files [34]. The first set of figures shown are heat maps representing block-average transmit gain measurements, created by averaging the gain patterns of the individual satellites within each block to create an average pattern for that block. These plots represent the final *level 5* products, incorporating all post-processing discussed in the previous section. GPS ACE measurements are plotted between 16 and 90 degree off transmitter boresight. The 16 degree off-boresight angle mask at a HORP altitude of approximately 1,200 km, removes measurements perturbed from passing close to the limb of the Earth.

Figures 11 and 12 show side-by-side comparisons between the GPS ACE reconstructed patterns and ground-based gain pattern measurements [5] for Block IIR and IIR-M, respectively. It is immediately apparent that GPS ACE reconstructed antenna patterns demonstrate excellent agreement with the antenna patterns measured by Lockheed Martin before launch, with both gross and fine-scale features common to both data sets.

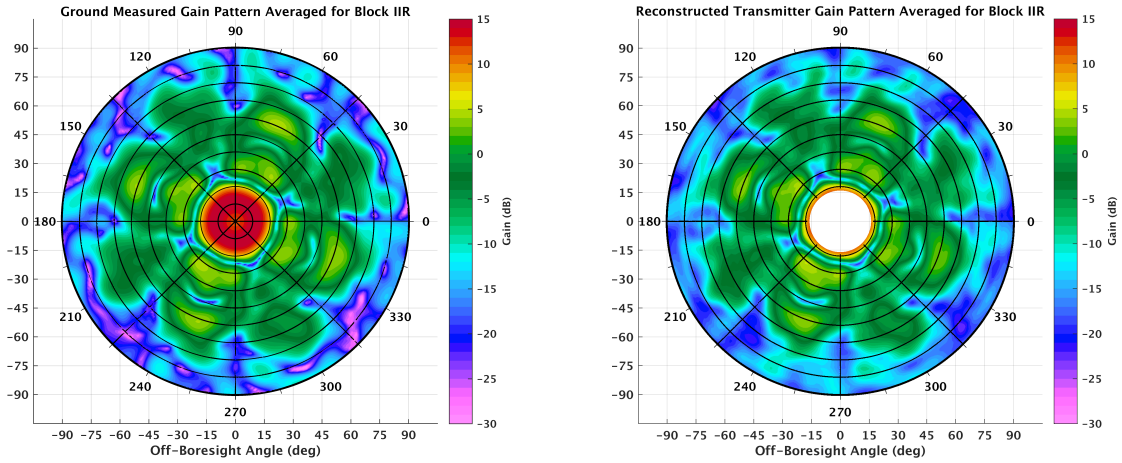

(a) (b)

Figure 11: Comparison of **Block IIR** ground measured antenna pattern (a) [5] to reconstructed antenna pattern from GPS ACE flight data (b) as heat maps to 90 degree off boresight.

Two major differences are visually apparent between the ground-measured and reconstructed patterns. First, the reconstructed data only contains the outer edge of the main lobe signal, due to the reception geometry at GEO and the applied 16 degree off boresight angle mask. Second, the ground-measured patterns feature deeper antenna nulls than the reconstructed patterns. This is most apparent by comparing the outer edges of each plot, near 90 degree off boresight angle. Figure 13 shows an azimuth cut from SVN 56 to illustrate the difference: there is a deep null in the ground measured pattern that is not entirely captured in the reconstructed pattern. There are multiple potential causes. Review of one of these areas in the observation data identified measurements in the 20 dB deep null, but found that the null was captured at different epochs at slightly different angles, causing it to be smoothed out in the reconstruction. Other potential factors include limitations of the MGPSR receiver to track through

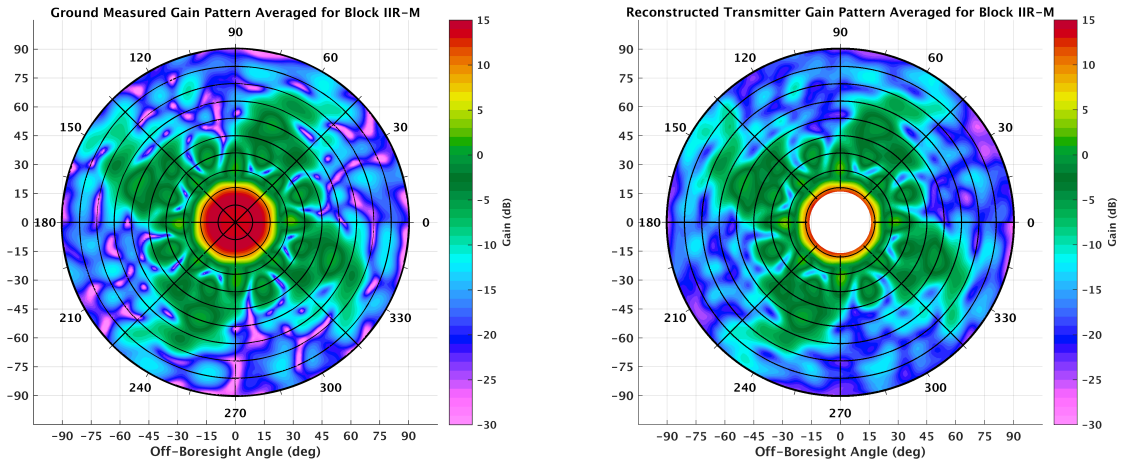

(a) (b)

Figure 12: Comparison of **Block IIR-M** ground measured antenna pattern (a) [5] to reconstructed antenna pattern from GPS ACE flight data (b) as heat maps out to 90 degree off boresight.

the deepest nulls; the choice to use 1 degree bin size, which results in a greater bin area near the edge of the pattern; and temporal variations in the null placement in the pattern itself or small deviations in the GPS satellite yaw angle.

It is important to note that the lack of deep nulls in the reconstructed data did not affect the normalization vs. ground-measured data, since this normalization was performed using elevation cuts from 16 to 23 degree off-boresight angle. Because most space-based GPS receivers cannot track through these deep null regions, the shallower nulls are not expected to impact future analyses using these results.

As can be seen in the following figures, sufficient GPS measurements were recorded from very weak GPS signals to completely reconstruct the full block-average patterns, and most individual SVN patterns, to 90 degree off-boresight. This data has previously only been available for Blocks IIR and IIR-M. As expected, the highest gain values are associated with main lobe region within approximately 23 degree of the transmitter boresight. The highest side lobe signals generally have 10–15 dB lower gain than the peak main lobe gain. The IIR satellites have the highest peak side lobe gain of any of the GPS satellite blocks. Comparing IIR (Figure 11) and IIR-M (Figure 12) patterns, it is apparent that the modernized

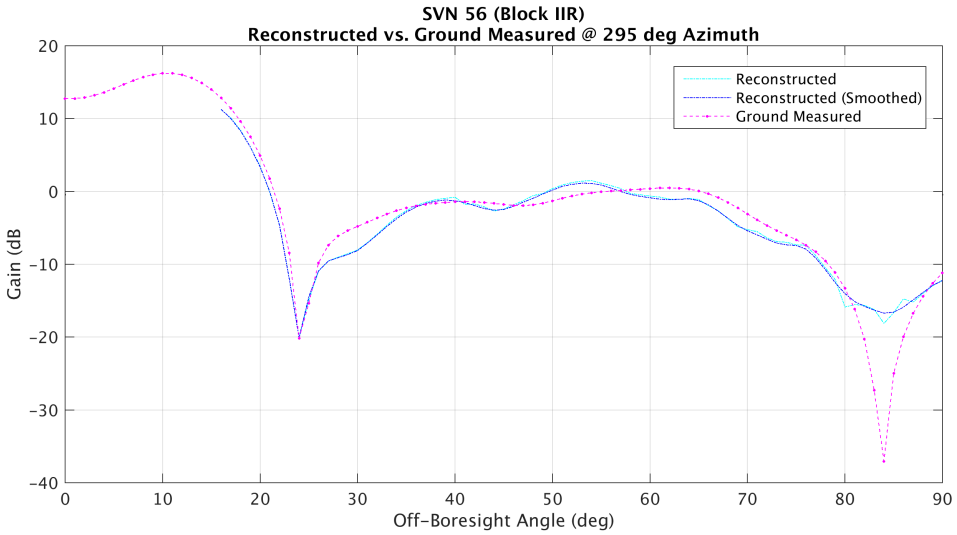

Figure 13: Example comparison of reconstructed antenna pattern vs. ground measured data from a Block IIR (SVN 56). This shows how the nulls in the reconstructed data are shallower than the ground measured pattern.

IIR-M antenna panel design suppressed the gain of the side lobe signals to optimize gain in the main lobe.

Figure 14 provides block-average reconstructed antenna patterns for GPS IIA and GPS IIF satellites. It is interesting to note that the Block IIF gain patterns are very similar to Block IIA, except that the pattern is clocked with a 45 degree relative offset. The similarities are expected, as both blocks were produced by Boeing. Also, no ground-measured data has been publicly released for the Block IIA satellites, and only limited data has been made available to the authors for Block IIF, so no direct comparison is presented here.

Figures 15 and 16 provide Cartesian plots of GPS ACE block-average gain versus elevation angle at regular azimuth cuts, illustrating more clearly the quantitative variation in gain across different azimuthal cuts.

In Figure 17, a comparison of the reconstructed pattern vs. the ground measured data for SVN 56 for an off-boresite cut at 30 degrees (first side lobe) shows that the detailed variations in azimuth are captured

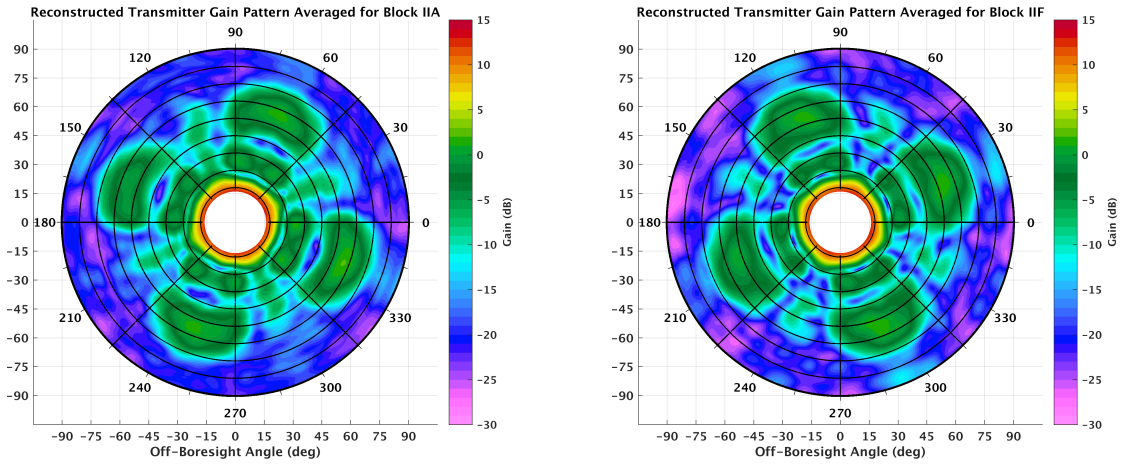

(a) (b)

Figure 14: Comparison of **Block IIA** reconstructed antenna pattern (a) to **Block IIF** reconstructed antenna pattern (b) from GPS ACE flight data as heat maps out to 90 degree off boresight.

in the recostruction process. This provides confidence in the reconstruction process for the Block IIA and IIF data for which the ground measured data is not available in the side lobes.

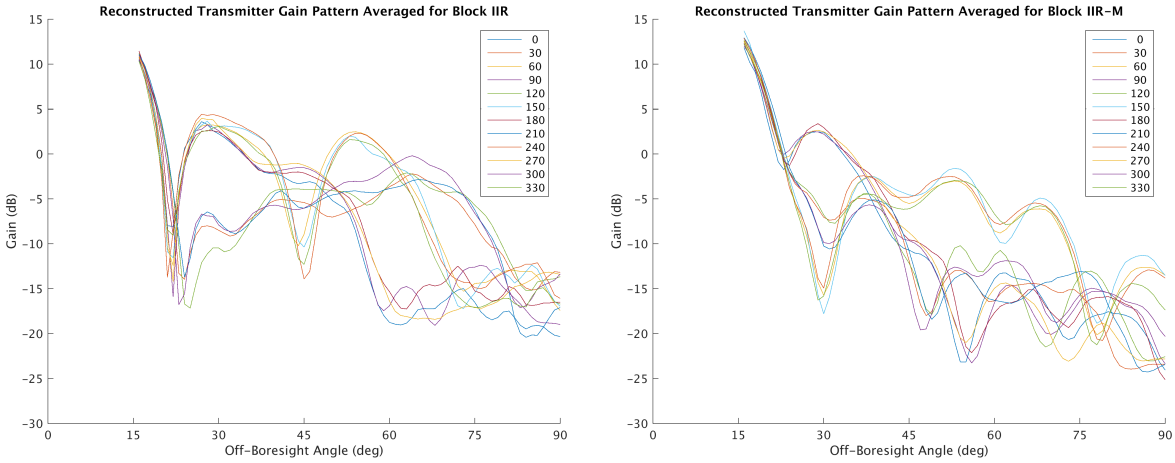

(a) (b)

Figure 15: Comparison of **Block IIR** reconstructed antenna pattern (a) to **Block IIR-M** reconstructed antenna pattern (b) from GPS ACE flight data as azimuth cuts every 30 degrees.

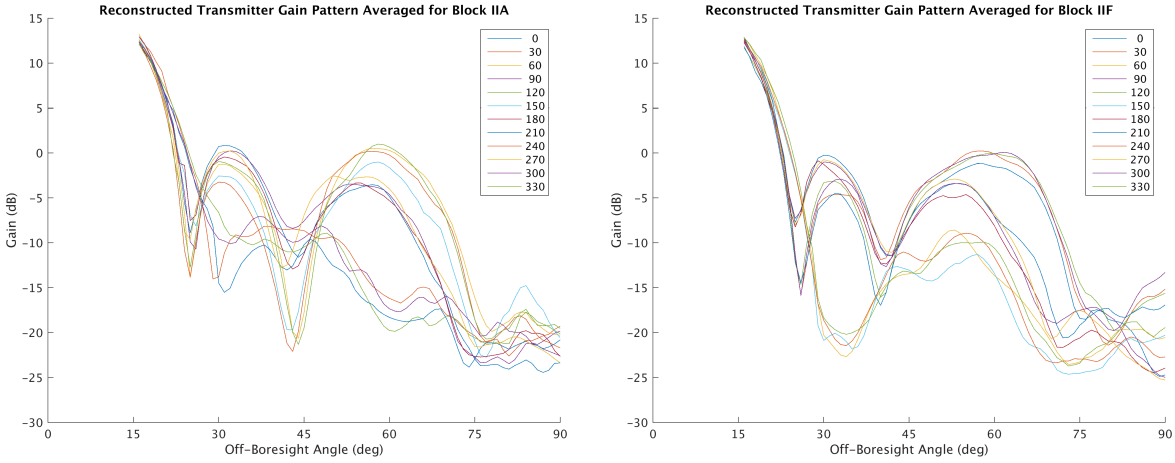

(a) (b)

Figure 16: Comparison of **Block IIA** reconstructed antenna pattern (a) to **Block IIF** reconstructed antenna pattern (b) from GPS ACE flight data as azimuth cuts every 30 degrees.

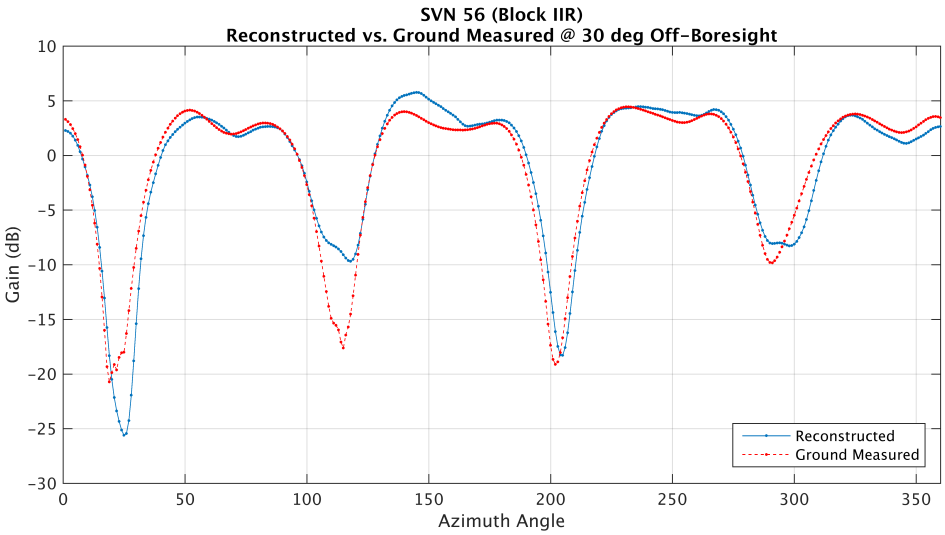

Figure 17: Example comparison of reconstructed antenna pattern vs. ground measured data from a Block IIR (SVN 56) using an off-boresight cut at 30 degree (first side lobe).

5.2 Comparisons Between Block Average and Individual Gain Patterns

Comparisons were made between the block-average antenna patterns and individual reconstructed patterns for each SV within the block.

This analysis demonstrates that variations in gain from SVN to SVN within a block are largely not significant. Figure 18 shows that the reconstructed block-average patterns closely match the individual reconstructed patterns to approximately 75 degree off boresight, which indicates that there are no large variations in the majority of the antenna patterns between individual satellites within a block. These results indicate that for constellation modeling and analysis purposes, block-average patterns can generally be used in place of modeling the side lobe shape of each individual satellite.

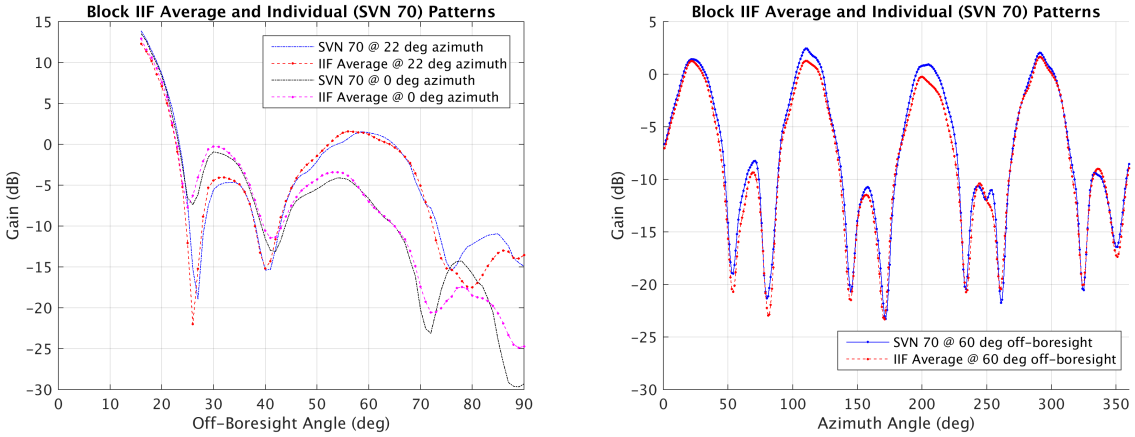

(a) (b)

Figure 18: Comparison of the **Block IIF** average reconstructed pattern vs. an individual **SVN 70** reconstructed pattern. Plot (a) shows two azimuth cuts at 22 degree and 0 degree. Plot (b) shows the azimuth variation at 60 degree off-boresight (second side lobe).

However, it was found that there do exist some mean differences in gain between patterns (before normalization). Because a fixed transmit power was applied uniformly to each block in the link budget, these differences represent both the uncertainty in the link budget calculations, which are discussed in greater detail in Section 6.2, as well as any actual differences in transmit power between individual satellites within a block. Figure 19 shows the mean difference across the entire pattern for each GPS

satellite vs. a reference vehicle in the block, along with mean and 3σ statistics across the set of differences. The plot shows that in general, differences in gain between SVNs within the same block average about 0.2 dB, and most are under 0.75 dB. SVN 70 and 73 are clear outliers compared to the other Block IIF SVNs, which may be an indication of higher transmit power on those satellites. Without those two SVNs, the average differences between SVNs across the blocks are less than 0.1 dB.

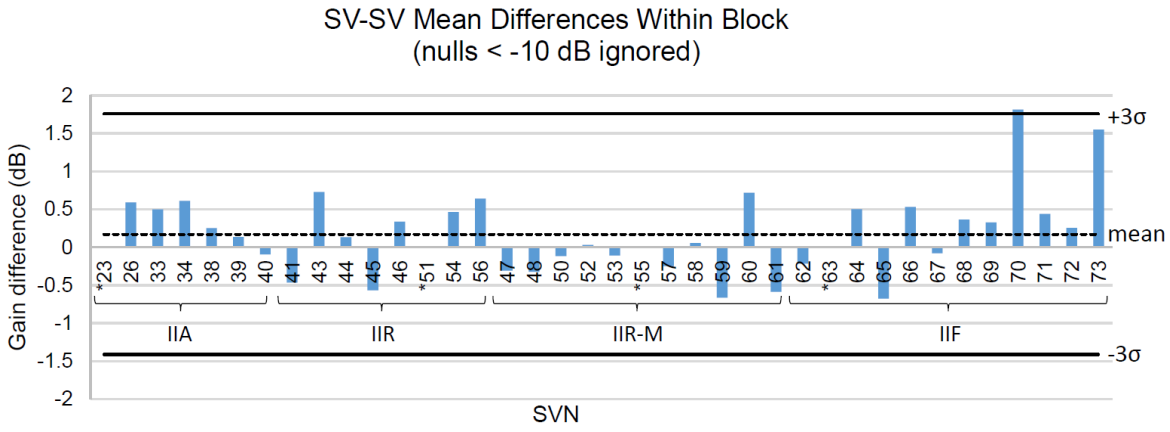

Figure 19: Mean gain differences between individual SVN patterns within each block, excluding deep (lower than -10dB) nulls. SVNs used as references are marked with (*). Block IIR-M includes IIR SVNs with the modernized antenna panel. The overall mean and 3σ lines are taken across the set of SV-SV differences.

6 Verification

This section describes the analysis performed to verify the reconstructed gain patterns and identify anomalous features in the data.

6.1 Data Editing

There are effects that cause errors and anomalies in the dataset. This subsection describes how that data was identified and removed from the full dataset.

6.1.1 Spacecraft Attitude

As mentioned previously, because the yaw behavior of the GPS satellites is not well defined during noon and midnight turns, the data collected during these periods are not included in the antenna pattern reconstruction process. In order to verify that the yaw model correctly identifies the period of time during which the spacecraft attitude is ill defined, spot checks were performed for SVNs 34 (Block IIA) and 61 (Block IIR). The received C/N_0 values were plotted for each SV for a 5 hour window during which an eclipse was predicted to occur and the receiver was tracking a strong side lobe signal. The GPS satellite attitude maneuver was clearly identifiable during both the shadow and post-shadow period as a variation in received signal power with fluctuations of up to 25 dB as the spacecraft presented a series of large nulls in the side lobes. As an example, Figure 20 shows a midnight turn of SVN 34. This check verified that all data points received during these attitude maneuvers are properly discarded by the yaw edit logic before generating the reconstructed antenna patterns.

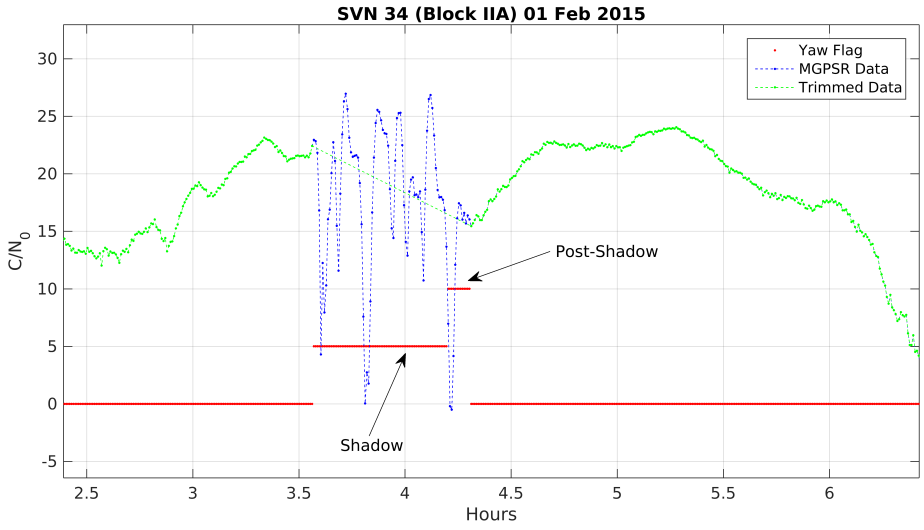

Figure 20: SVN 34 Block IIA Received C/N_0 over a midnight turn (eclipse).

6.1.2 Ground Configuration Changes

The MGPSR receiver has been nearly continuously processing the digitized GPS signals for several years. Inevitably, parts of the ground system upstream of the RF digitizer are occasionally brought off-line or have undergone some other configuration changes. These configuration changes could introduce errors in the dataset when they occur. The dates and times of these changes are recorded and were available to edit out bad data. Because the MGPSR processes the digitized signal in two hour chunks, when a change occurs, the two hour data set is corrupted. The MGPSR then automatically adjusts to match the current ground system configuration for the next two hour period. Spot checks were performed for every type of configuration change experienced over the data collection period. These checks consisted of plotting the received C/N_0 during each event and inspecting the quality of the data during those time periods such as looking for outliers or non-physical behaviors. Figure 21 is an example of one such spot check. It was found that the time stamps associated with configuration change logs were only accurate to within approximately 5 min of the actual start and stop times as observed in the plots. Therefore, all data 15 min before a recorded configuration change is discarded before generating the reconstructed antenna patterns. The 15 min was verified to be sufficient margin by spot checking several configuration changes.

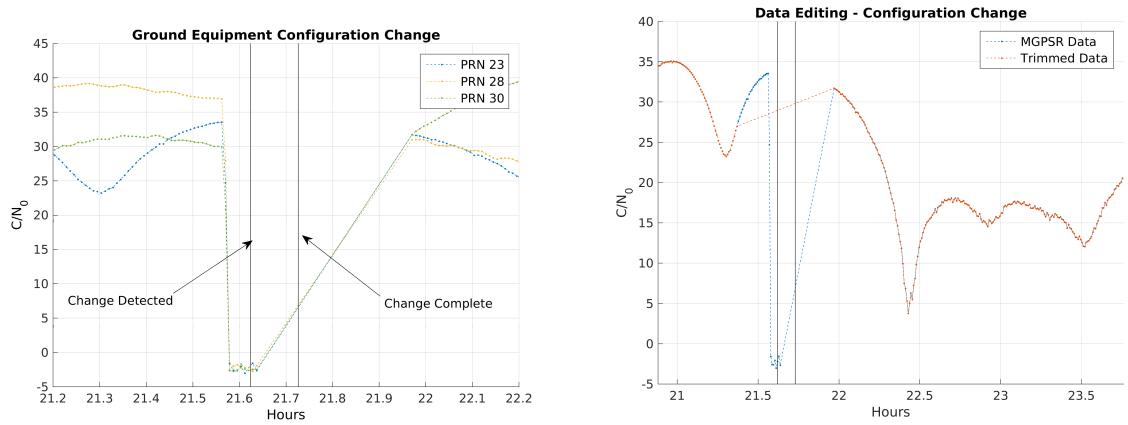

(a) (b)

Figure 21: Received C/N_0 over a ground equipment configuration change. Plot(a) shows a sample of the signal drop for three PRNs. Plot (b) shows the pre and post-edit data sets for one PRN. A conservative margin was used. In this particular case, data was masked 15 minutes before the stated time of the configuration change until the end of the 2 hour arc.

6.1.3 Anomalous Tracking Data

From one day to the next, the C/N_0 profile as a function of time for a particular GPS SV does not change significantly because of the unique geometry between the GEO receiver and the MEO GPS transmitters. That repeatability can be exploited to do additional data integrity spot checks on the received C/N_0 data. Occasionally, the MGPSR receiver will have a bad tracking pass for 2–4 hours. The root cause is not always known, however, the possibilities include cross-correlations and unplanned GPS spacecraft activities such as off-nominal spacecraft yaw attitudes. Examination of plot (a) in Figure 22 shows one such example where the tracking pass on one day appears to represent an off-nominal behavior of the SV and the next day the pass looks clean. It was confirmed by the GPS operators that on this particular day for SVN 62, this behavior was caused by a 20 degree yaw bias applied to the spacecraft around local dusk. Since it would not be possible to catch all such events manually, an automated process for detecting and removing this data was developed. In addition to the C/N_0 and pseudorange measurements reported at the end of each two hour data processing batch, the MGSPR outputs information on the

pseudorange measurement error standard deviations, σ_m, and estimated ionospheric delay correction, d_i, both of which can be used to find outliers. If σ_m has a large jump while the receiver is tracking strong signals ($C/N_0 > 25$ dB-Hz), it is an indication that there may be bad data. Additionally, if the receiver reports very weak signals ($C/N_0 < 5$ dB-Hz) for a long period of time when the d_i correction flag is low, i.e., the signal is not being attenuated by the atmosphere, then the data is also flagged as anomalous. Plot (b) in Figure 22 shows the same Day 1 with the bad pass in the left plot for a longer 8 hour arc and demonstrates how the automated process was able to detect and flag the data that needed to be discarded. It should be noted that while the d_i and σ_m flags could also be used to remove the main lobe data that is attenuated by the atmosphere, it was decided that this data should be removed after the final antenna pattern reconstruction using an angle off-boresight mask corresponding to the height of the Earth's ionosphere as seen from GEO, rather than in the pre-processing.

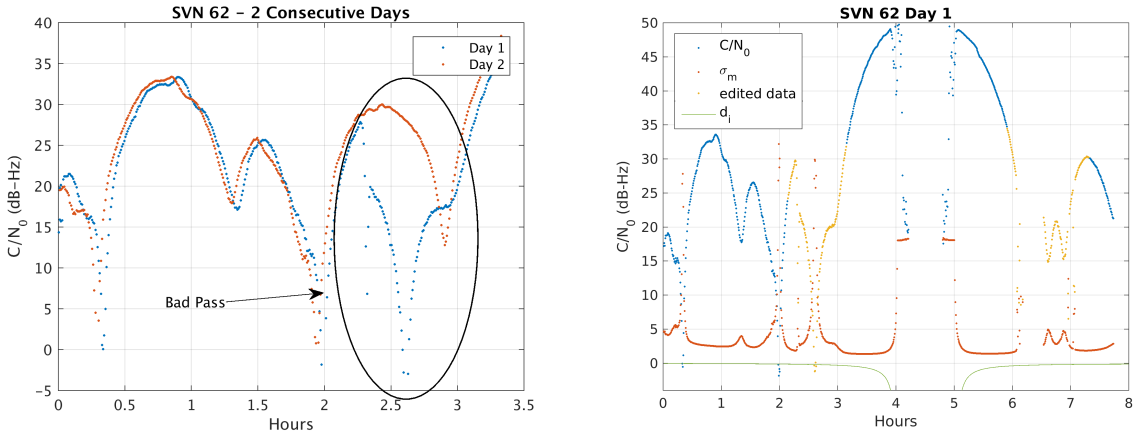

(a) (b)

Figure 22: Plot (a): Received C/N_0 on two consecutive days for SVN 62 where the Day 1 data appear to have a discontinuity at around 2.25 hours into the day caused by a yaw maneuver. The Day 2 data look nominal. Plot (b): Received C/N_0 for an 8 hour arc on Day 1 for SVN 62. The automated data editing process found the bad pass at hour 2.25 and another bad pass starting at hour 5.75.

To aid in identification of outliers, a custom tool called `PatternExplorer` was developed for interactive interrogation of the final antenna pattern products. This tool allows the user to load a product, usually a level-0 gain plot, interactively focus on specific features of the pattern, select individual bins of

measurements, see measurement statistics and distribution details, and perform per-bin sigma-editing experiments. It also enables interactive interrogation of specific measurements back to the source data for investigation of outliers and other features. The `PatternExplorer` interface is shown in Figure 23.

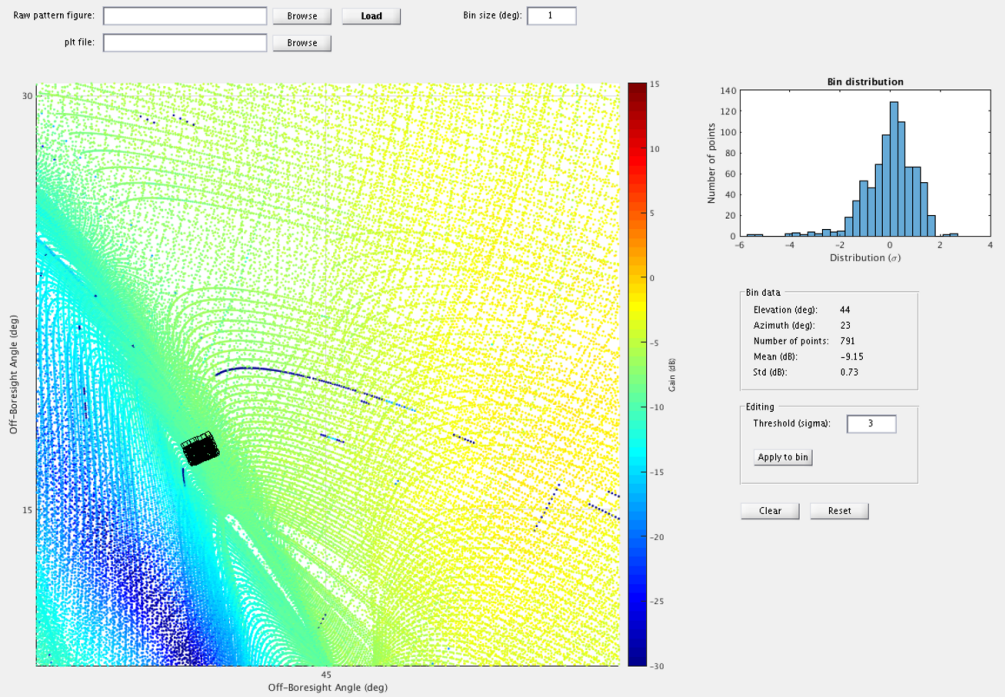

Figure 23: The interface of the `PatternExplorer` tool, showing interrogation of an individual bin of raw unedited measurements (black dots in lower left of pattern) and associated statistics.

6.2 Link Budget Summary

There are several sources of error in the GPS ACE antenna pattern reconstruction link budget. As described in Section 4.3 and shown in Eq. 14, the measured carrier to noise density ratio C/N_0, noise temperature of the system, N_0, and the receive antenna gain, A_r, are required to determine the transmitter gain. These are the largest sources of error in the link budget and are discussed in greater detail in the following sections.

6.2.1 Uncertainty in Carrier to Noise Density

The MGPSR algorithm for estimating the carrier to noise density ratio was presented in Section 3.2.3. One method of determining the uncertainty in the MGPSR C/N_0 calculation is to compare the MGPSR measurements to the Navigator GPS receiver outputs for the same pass. Since the Navigator is not as sensitive as the MGPSR, a main lobe pass was chosen for this analysis. The Navigator C/N_0 estimator is a measurement of the ratio of narrow-band power to wide-band power (see Ref. [32] p. 391), which is very similar to the MGPSR method. The Navigator receiver applies a low-pass filter to the output, which results in a less noisy measurement. A comparison of the C/N_0 outputs of the two receivers is shown in Figure 24. A third-order polynomial was fit to the two data sets and the fit residuals were plotted to show the relative uncertainties in the two C/N_0 outputs. The standard deviation of the Navigator fit residuals was 0.224 dB, and the standard deviation of the MGPSR fit residuals was 0.665 dB.

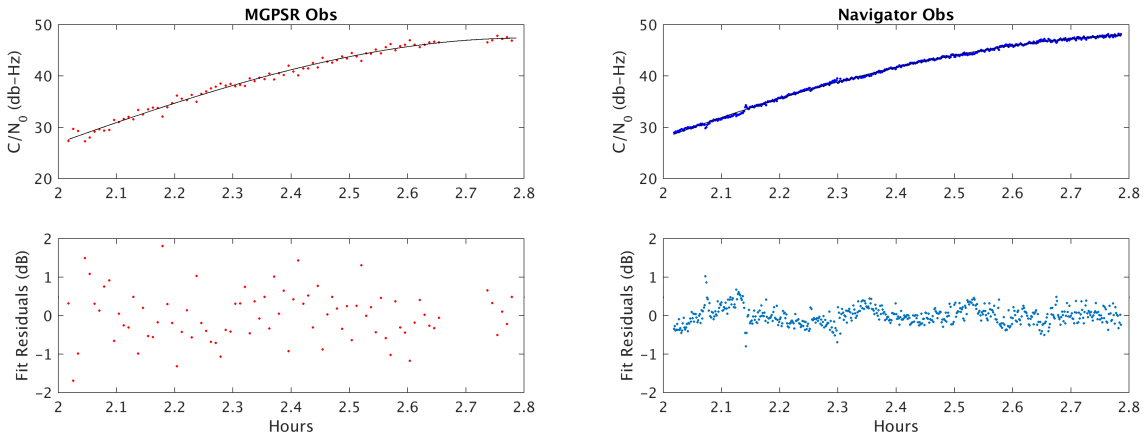

Figure 24: A comparison of MGPSR (a) and Navigator (b) received C/N_0 during one pass in the mainlobe with a third-order polynomial fit and fit residuals.

In addition to the variation in the C/N_0 estimate, there may also exist a mean error in the estimator output. While there is no way to determine if such an error exists by analysis of the GPS ACE data, there is a detailed discussion of the estimator performance in [6] which describes both the mean and standard deviation of the Navigator C/N_0 estimator as a function of C/N_0. As shown in [32] the error

in the mean grows from approximately 0.25 dB at a C/N_0 of 30 dB-Hz to 1.2 dB at 10 dB-Hz. For the GPS ACE data set, this effectively means that there is a greater uncertainty in the shape and depth of the null regions of the reconstructed antenna patterns than there is in the stronger main and side lobes.

6.2.2 Uncertainty in the Noise Temperature of the Receiver

Another source of uncertainty in the GPS transmit antenna pattern reconstruction link budget is the calculation of the receiver noise density. The receive antenna noise temperature is a function of the integrated temperature over the entire aperture. This temperature is a function of the variation in temperature across the Earth disk and the changing attitude of the spacecraft. The contributions of the Sun and Moon in the antenna field of view were also ignored because it was found that, in the average, they did not change the noise temperature of the system significantly, and it was determined that the pre-binning data editing described in Section 4.4 removed the local outliers. Additionally, the total system noise temperature is a function of multiple elements, only the two largest of which were modeled: the LNA and the downconverter. This error is assumed to be fixed but is unknown. For example, an error in the system noise temperature of 25 K results in an error of approximately 0.6 dB in the calculation of noise density.

6.2.3 Uncertainty in the Receiver Antenna Gain Pattern

An additional source of uncertainty in the link budget is the uncertainty in the knowledge of the receive antenna pattern. The data available to the GPS ACE team were measurements of the antenna pattern at nine equally spaced elevation cuts and around the azimuth from 0 to 45 degrees off-boresight angles at 3 degree steps. The azimuthal variation in the pattern as a function of off-boresight angle increased to almost 10 dB at 45 degree off-boresight. This variation required interpolation of the antenna pattern data in two dimensions so that the actual receiver gain values could be computed for any received signal geometry. The original approach was a simple two-dimensional interpolation in angle space. However, upon closer inspection, that method proved to have several flaws. First, because the antenna data

is sparse in azimuth at the lower elevation angles, linear and spline interpolation were not accurate in those regions. Additionally, interpolation in angle space instead of Cartesian means the that information connecting data at 0 degree azimuth and 359 degree azimuth was lost, creating larger errors in that region of the pattern. Instead, the antenna pattern data was converted from polar azimuth and elevation angles to Cartesian x, y pairs and then a surface was fitted to the data using a biharmonic gridded data method. This created a smooth surface to sample antenna gain at any received signal geometry as shown in Figure 25.

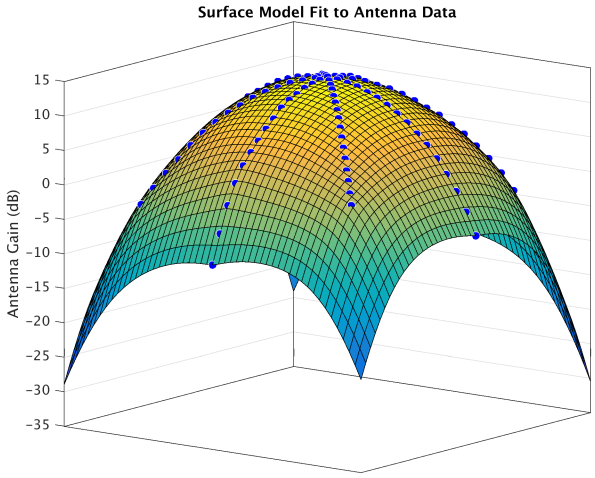

Figure 25: Smooth surface fitted to sparse receive antenna gain data.

6.3 Other Error Sources

Other error sources were considered in the verification process, including:

- Orbit/attitude ephemeris error
- GPS ephemeris (almanac) error
- Orbit/attitude interpolation error
- GPS yaw error
- Coordination system transformation error (e.g., error in FK5 reduction)
- Floating-point round-off error

To evaluate the significance of these errors, the limits of acceptable error in a given measurement were determined based on an error threshold in the final link budget of 0.1 dB in gain and 0.5 degree in transmit antenna azimuth/elevation position. These thresholds were chosen as error bounds on the individual contributions to the total error to minimize impact on the final products. Using the link budget path loss and angular offset calculated at the smallest possible range between transmitter and receiver, the radial, in-track, and cross-track position errors were calculated that would cause a link budget error in excess of these thresholds. The calculated errors were estimated to be well in excess of the expected combined error in all of the above sources.

The attitude error around boresight for both the receiver and transmitter is more directly mapped to an angular error on the final transmit pattern. These models were verified individually for correctness, and known intervals of greater uncertainty, such as GPS satellite shadow periods, were excluded. The presence of systematic angular biases was investigated during comparison with ground-test data at a pattern level, and none was found.

Because there are several sources of uncertainty in the link budget calculations, such as assuming a constant GPS signal transmit power, it is difficult to quantify the total error in the reconstructed data. One way to evaluate the accuracy of the reconstructed antenna patterns is to use those patterns to simulate expected GPS signals and then validate those simulations with measured flight data. In a paper published in 2019, Winternitz [35] used that process with the GPS ACE reconstructed patterns with flight data from MMS phase 2B orbit. The GPS ACE antenna patterns were able to accurately predict the signal levels seen by the MMS spacecraft, providing an independent calibration source used to validate the GPS ACE results. This provides strong evidence that while the individual error contributions are unknown, the overall accuracy of the reconstructed patterns is sufficient for use in the intended application.

7 Pseudorange Deviations

The preceeding sections have discussed GPS signal availability for GEO and HEO applications. Next, we address the signal quality at these high altitudes. Much work has been done for low-Earth orbit applications and for geodesy applications [36, 37]. We also mention the SVN-49 signal anomaly because it provided an exceptional case of the variation of the signal delay with elevation [38]. In this paper, we use the term *pseudorange deviation* instead of *group delay* to address variations in the measured pseudorange with GPS boresight angle. The term pseudorange deviation has been introduced by Dybdal to address systematic differences between the pseudoranges determined from an actual GPS system and an ideal system [39]. The objective here is to assess systematic deviations in the pseudorange with the GPS boresight angle and azimuth at the large boresight angles in the SSV.

The expectation is that an assessment would be possible in the primary sidelobes of the shaped beam antenna pattern [40], and that the pseudorange deviations would be benign. However, outside of the primary sidelobes and in the nulls between the sidelobes, any measureable response would exhibit large deviations and have high levels of noise. In those regions, multiple scattering interactions would predominate, diminishing the utility of any detected signal.

7.1 Approach

The Aerospace Corp. high fidelity orbit determination tool TRACE is used with the post-fit ephemeris of the GEO satellite and NGA precise phase-center ephemeris and clock for the GPS constellation to create pass-through pseudorange residuals for all observations. Residuals are edited and binned in the same manner as in the gain pattern processing, resulting in a mean residual in each 1 degree bin.

This mean residual is taken as an estimate of the pseudorange deviation δ_{PD} at each particular GPS off-boresight and azimuth angle.

If the mean residual $\bar{b}$ in a bin can be expressed as

$$\bar{b} = \frac{1}{n}\sum_{i=1}^{n}(\eta_0 + \eta_m) + \delta_{PD} \tag{15}$$

where η_0 and η_m represent zero mean model and measurement errors, respectively, then for a sufficient number of samples the mean residual in a bin will be an estimate of the pseudorange deviation δ_{PD} at that boresight angle and azimuth.

Specific modeling compensation accounted for in TRACE includes GPS receive antenna and downlink antenna location offsets from the GEO satellite center of mass, GEO satellite attitude, precise ground station location, and internal GEO satellite and ground path delays. The remaining effects such as phase center variations of the L-band antenna panel shaped beam elements or element interaction are assumed to contribute to variations in the L-band signal causing systematic devations in the measured pseudorange. These deviations generally result from the GPS receiver correlator/discriminator response to distortions in the correlation function, and the response is dependent upon the correlator/discriminator design as discussed in Ref. [39]. In this regard, the MGPSR is a multitap receiver using many samples of the CA-code correlation function in each measurement and may not represent the performance of a early-late-prompt correlator receiver.

As stated above, the pseudorange residuals are computed using the GEO satellite post-fit ephemeris, which does not use weak signal GPS observations in the orbit determination. This largely isolates the results from correlations due to fitting all the subject observations. In fact, post-fit residuals improve if TRACE is used to also solve for the ephemeris. However, since no weak signal GPS observations are used in the GEO satellite ephemeris determination, residuals at large GPS off-boresight angles are not included in the minimization process and, thus, represent a fair assessment of the pseudorange deviation.

7.2 Results

7.2.1 Residual Noise Correlation with Signal Strength

Since the MGPSR can process the weakest signals, it is important to understand the correlation between pseudorange residual noise and received C/N_0. Figure 26 shows the mean (top) and standard deviation (bottom) of the raw pseudorange residuals versus received C/N_0 for each block based on the pass-through

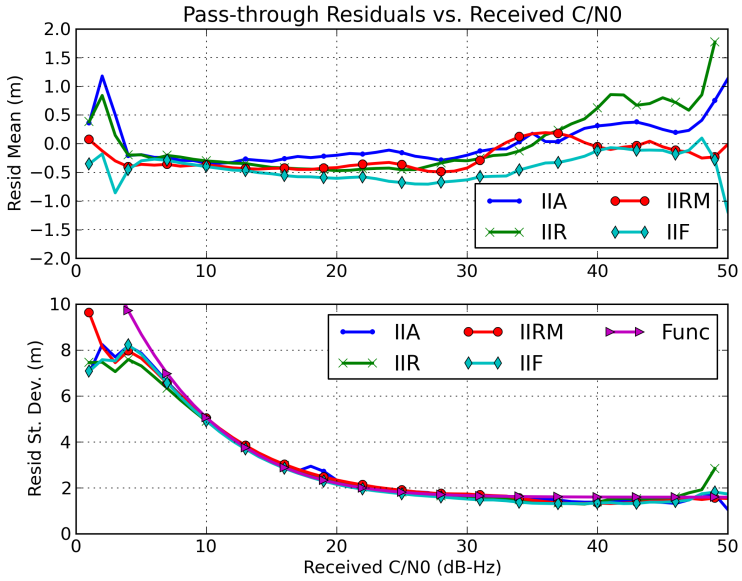

Figure 26: Pass-through pseudorange residual mean (top) and standard deviation (bottom) vs. received C/N_0.

analysis. The values are created by sorting residuals into 1 dB-Hz bins and taking sample statistics on each bin. The mean values have not been normalized, but they are generally within 1 m at all but the extreme signal levels. The spread in the mean at high signal levels is likely due to biases caused by atmospheric effects on main lobe transmissions. For a receiver at GEO, only the main lobe signals pass through the Earth's atmosphere.

The standard deviation plot shows that all blocks exhibit remarkably similar pseudorange noise. As expected, measurement noise increases as signal level decreases. A relationship can be determined to model the measurement noise as a function of signal level—a useful tool for relative weighting of pseudorange in the orbit determination process. From Ref. [25], the relationship is

$$\sigma_{PR} = 1 \times 10^{-6}\, c \left[\frac{1}{1.8B} \frac{1}{\sqrt{SNR}} \right] \tag{16}$$

where σ_{PR} is the pseudorange noise in m, c is the speed of light in m/s, SNR is the signal-to-noise ratio of the received signal, and B is the effective signal bandwidth in MHz. The SNR is related to the C/N_0 through Eq. 5 where $SNR = P - 1$, T is the integration time in seconds, and C/N_0 is expressed in dB-Hz.

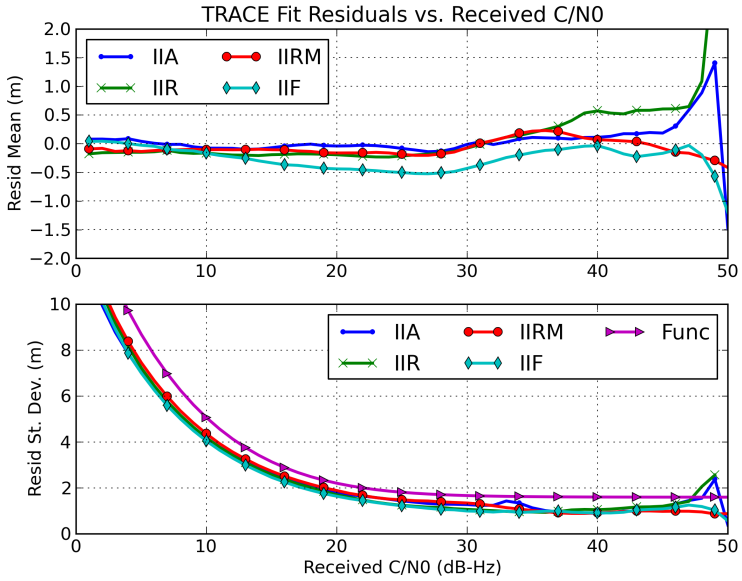

Figure 27: TRACE pseudorange residual mean (top) and standard deviation (bottom) vs. received C/N_0.

The Func line in the bottom plot of Figure 26 is the effective pseudorange noise which is the RSS of the SNR component and a model component. The effective pseudorange noise $\sigma_{PR_{eff}}$ can be modeled using a slight modification of Eq. 16, adding a bias to represent the noise floor,

$$\sigma_{PR_{eff}} = \sqrt{\sigma_{PR}^2 + \sigma_{floor}^2} \tag{17}$$

where σ_{floor} is an empirical noise floor determined from the data. In Figure 26, the $\sigma_{PR_{eff}}$ function is obtained using $\sigma_{floor} = 1.6$ m and $B = 2$ MHz to produce an envelope of the pseudorange noise at the MGPSR integration time of $T = 30$ s.

The residuals are reduced further by processing a subset of observations through Aerospace TRACE using only those observations with signal levels above 22 dB-Hz. Figure 27 shows the same quantities for the TRACE residuals as shown in Figure 26 for the pass-through analysis. The mean residuals show similar trends to those in Figure 26, but with slightly smaller offsets. The standard deviation plot shows the same $\sigma_{PR_{eff}}$ function as determined for the pass-through results, clearly demonstrating that the TRACE fit is able to reduce the noise floor. In this case, changing σ_{floor} to 1.0 m in Eq. 17 would bring the effective noise function down to the level of the TRACE fit. Computing an independent trajectory

estimation with strong side lobe signals and producing a similar, but lower noise fit provides confidence that the pass-through analysis represents a fair assessment of the pseudorange accuracy in the side lobes. To be more conservative, the remainder of the results in this section are generated from the pass-through analysis.

7.2.2 Block Average Performance

The small biases in the raw residuals shown in Figure 26 are strong indicators of the expected pseudorange deviation performance. Binning the raw residuals into a 1x1 degree grid produces an estimate of the pseudorange deviation from that location in the GPS transmit pattern. Among many ways to view the results, samples are given here of pseudorange deviation behavior across constant elevation, constant azimuth, and averaged at each off-boresight angle.

Figure 28 shows cuts at constant off-boresight angles for Blocks IIR-M and IIF. The cuts occur at 18 (top), 30 (middle), and 45 degree (bottom) off boresight. The 18 degree cut is in the GPS main beam, while the others are in the side lobes. While there is some variation in the mean residual correlated to the location of nulls, the overall bias and variability are relatively small. Compare the azimuth of features in these plots to their respective gain plots in Figures 12 and 14.

Given that the elevation cuts show relatively small variations, normalization of the residuals by the mean across all azimuths at a location in the main beam provides a relative measure of the deviation in the side lobes, assuming small deviation in the outer portion of the main beam. The following results are normalized by removing the block-average residual at 18 degree off boresight for each of the respective blocks. For example, the value removed for Block IIF is the mean of those values plotted in the top panel of Figure 28(b). The normalization constants for each block are shown in Table 5, but with about 0.5 m of noise as evidenced by the respective standard deviations. Note that the residuals are consistent with the biases at high C/N_0 values in the top plots of Figures 26 and 27.

Using the normalized results, Figure 29 shows azimuth cuts every 15 degrees out to 90 degrees off

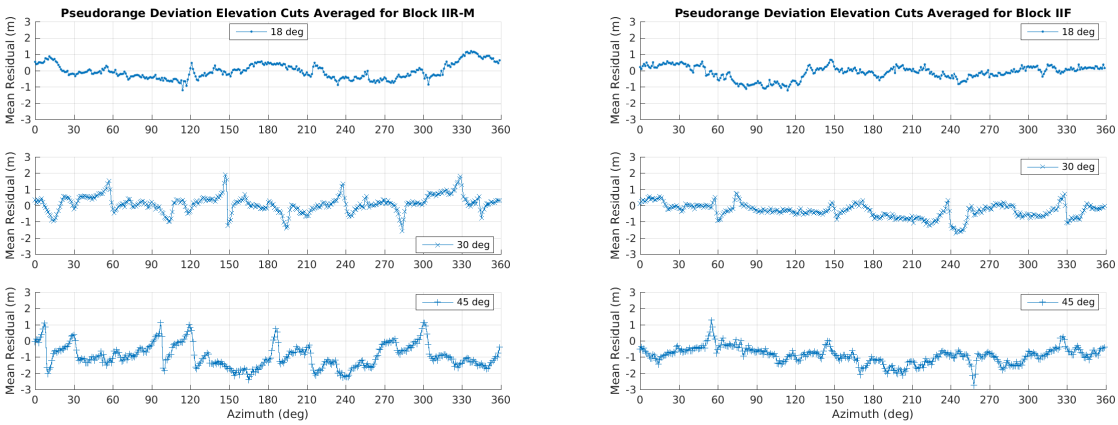

(a) (b)

Figure 28: Elevation cuts at 18, 30, and 45 degree off boresight for Block IIR-M (a) and Block IIF (b) average pseudorange deviations.

boresight for Block IIR-M and IIF. In these plots, the mean at 18 degree off boresight is zero. Clearly, some azimuths are noisier than others, again correlated to the signal levels. However, one feature that stands out is the general trend of all cuts towards a negative bias in the side lobes. Blocks IIA and IIR show similar trends.

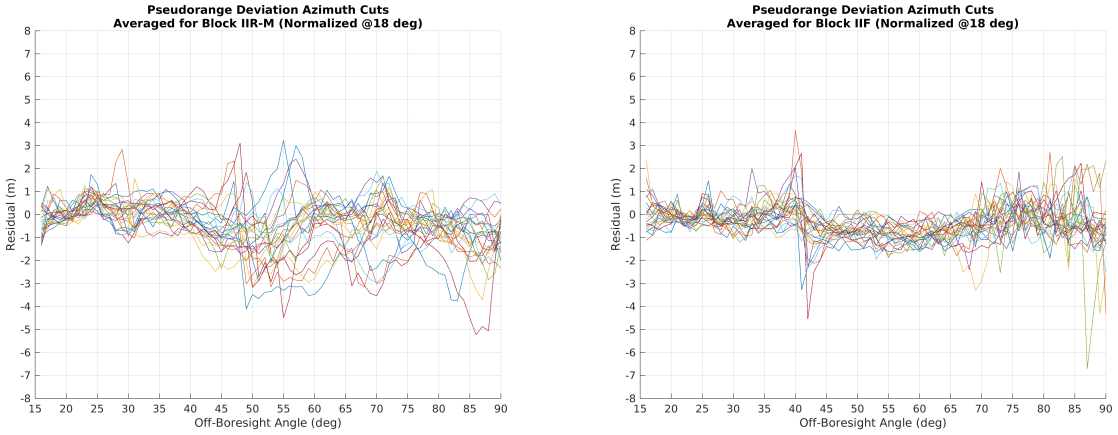

(a) (b)

Figure 29: Azimuth cuts every 15 degree for Block IIR-M (a) and Block IIF (b) average pseudorange deviations.

Table 5: Mean pseudorange residual and standard deviation at 18 degree off boresight for each block. Residual values are used for normalization. The IIR-M category includes IIR SVNs with the modernized antenna panel.

Block	Mean Residual at 18 degree off boresight (m)	Residual Standard Deviation at 18 degree off boresight (m)
IIA	0.36	0.60
IIR	0.58	0.53
IIR-M	-0.05	0.47
IIF	-0.13	0.41

Taking the mean at each elevation across all azimuths of the binned residuals for each of the four blocks results in Figures 30 and 31. The error bars represent the standard deviation of the means of the binned values at each off-boresight angle. Each figure has three subplots demonstrating the characteristics of the pseudorange deviation at different minimum received C/N_0 values: 0, 15, and 22 dB-Hz. For example, the middle plots in Figure 30 show the pseudorange deviation averaged over only those bins that have an average C/N_0 at or above 15 dB-Hz. If there are no bins at a given off-boresight angle that have a high enough signal level, nothing is plotted at that angle.

Each block shows a similar trend of a negative bias in the side lobes that remains consistent at the different signal levels. The cause of the negative bias is unknown. It could be GEO satellite ephemeris error, phase center variation of the GPS transmit antennas, or GEO satellite receive antenna, a systematic effect in the TRACE pass through analysis, etc. However, the key feature of these plots is the small pseudorange deviation into the back lobes. For most high altitude GPS users, a deviation of 1–2 m is in the noise of the orbit determination solution or below the navigation accuracy requirement. This is clear evidence that pseudoranges in the GPS side lobes are of sufficient quality to be useful for many HEO navigation applications.

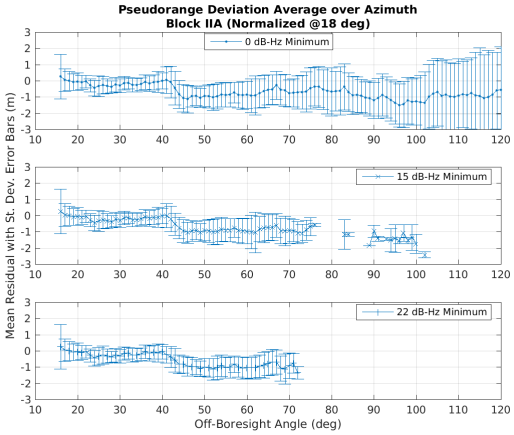

(a)

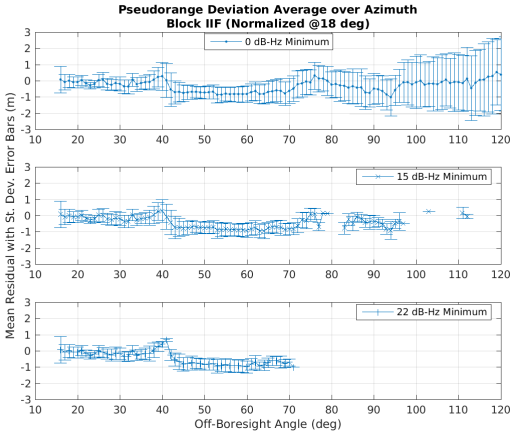

(b)

Figure 30: Block IIA (a) and Block IIF (b) pseudorange deviation mean over azimuth with standard deviation error bars.

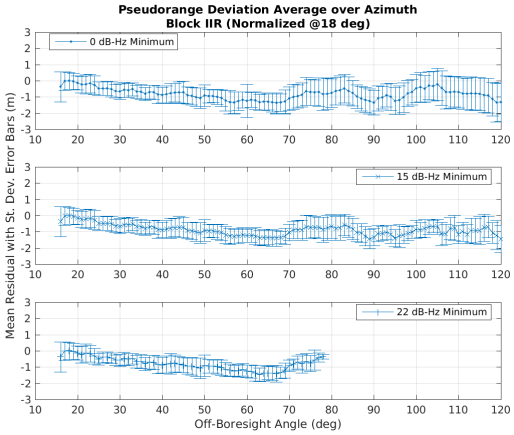

(a)

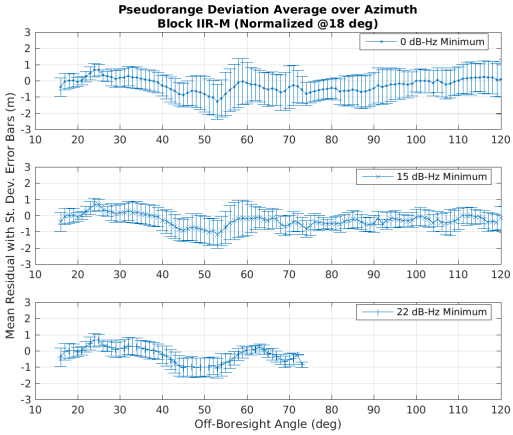

(b)

Figure 31: Block IIR (a) and Block IIR-M (b) pseudorange deviation mean over azimuth with standard deviation error bars.

8 Conclusions & Future Work

Extensive measurements of received GPS signal levels from a geosynchronous satellite recorded by the GPS Antenna Characterization Experiment have allowed comprehensive maps of GPS satellite gain and pseudorange deviations to be constructed for the entire GPS constellation for the L1 signal. Fundamental to the collection of this dataset was the Aerospace Mariposa GPS Receiver and the long duration of the experiment. With sensitivity to below 0 dB-Hz, the MGPSR provides continuous all-in-view tracking from the GEO spacecraft, and the massive GPS ACE dataset provides many redundant measurements to enable statistical analysis and aid in identification of outliers.

Comparisons between gain measurements reconstructed from GPS ACE data and those measured in ground testing for the Block IIR and IIR-M satellites show excellent agreement. This demonstrates the value of conducting careful characterization of the GPS satellite antennas prior to launch because, even in the side lobes, these ground measurements have been demonstrated to be representative of on-orbit performance. Furthermore, variations between individual GPS satellite gain patterns and the block-average patterns were found to be small outside of the deep null regions. This implies that analysts can safely use block-average gain patterns in their analysis and obtain realistic results.

This data set has provided insight into the pseudorange errors inherent in the side lobe signals, and has validated the suitability of side lobe transmissions for navigation. Range deviations constructed by generating pass-throughs of the measured pseudoranges with respect to the reconstructed orbit for the geosynchronous receiving spacecraft were found to be generally well below 2 meters. These results were obtained using a multi-tap correlator, and may vary with other receiver designs. Moreover, the range deviations exhibit a systematic pattern that would be conducive to applying a range deviation correction as a simple function of elevation to reduce the net error further.

The paper describes the extensive efforts taken through the post-processing of the data set to identify and remove erroneous measurements and other outliers, and to perform sensitivity analysis to characterize and quantify the various error sources inherent in the analysis of the data.

The GPS ACE reconstructed antenna patterns should allow precise modeling of GPS signal availability for HEO users, whereas in the past mission planners had to make conservative assumptions regarding the availability of side lobe signals and their inherent error characteristics. This improved modeling fidelity is especially important for more stressing future HEO GPS applications such as use of GPS on cubesats, in which a directional receive antenna is likely precluded, or in applications to human lunar exploration of the moon [41, 35]. Moreover this dataset will be invaluable to inform any changes that might be considered to GPS Space Service Volume (SSV) performance requirements in the future.

Looking to the future, the authors would like to further explore the extent of any temporal variations in transmitted power levels present in the data. There is also interest in utilizing the reconstructed antenna patterns and the ODTBX modeling software to compare observed vs. predicted GPS receiver power levels for additional operational missions such as GOES. There is also interest in refining the knowledge and the limitations of the GPS vehicle yaw models using the GPS ACE data. As GPS III satellites are added to the GPS constellation in the near future, it is expected that GPS ACE data will be used in an on-orbit assessment of the performance of those satellites and to produce gain and pseudorange deviation data plots.

9 Antenna Pattern Data Availability

The antenna patterns and associated metadata can be accessed at the following location:

`https://esc.gsfc.nasa.gov/GPS_ACE`

10 Acknowledgment

This work was performed under a collaborative Independent Research and Development effort between The Aerospace Corporation and NASA Goddard Space Flight Center authorized under Space Act Agreement SAA5-14-2-N16999.

References

[1] Winkler, S., Ramsey, G., Frey, C., Chapel, J., Chu, D., Freesland, D., Krimchansky, A., and Concha, M., "GPS Receiver On-Orbit Performance for the GOES-R Spacecraft," in *10th International ESA Conference on Guidance, Navigation & Control Systems, Salzburg; Austria*, 2017.

[2] Winternitz, L. B., Bamford, W. A., Price, S. R., Carpenter, J. R., Long, A. C., and Farahmand, M., "Global Positioning System Navigation Above 76,000 km for NASA's Magnetospheric Multiscale Mission," *NAVIGATION*, vol. 64, pp. 289–300, Summer 2017.

[3] Winternitz, L. B., Bamford, W. A., and Price, S. R., "Navigation Results from the Magnetospheric Multiscale Spacecraft and Simulations at Lunar Distances," in *Proceedings of the 30th ION GNSS+*, (Portland, OR), September 2017.

[4] Bauer, F., Moreau, M. C., Dahle-Melsaether, M., Petrofski, W., Stanton, B., Thomason, S., Harris, G., Sena, R., and Parker Temple III, L., "The GPS Space Service Volume," in *Proceedings of the 19th International Technical Meeting of the Satellite Division of The Institute of Navigation (ION GNSS 2006)*, pp. 2503–2514, September 2006.

[5] Marquis, W. and Reigh, D., "The GPS Block IIR and IIR-M Broadcast L-Band Antenna Panel: Its Pattern and Performance," *NAVIGATION*, vol. 62, pp. 329–347, Winter 2015.

[6] Winternitz, L. M., Bamford, W. A., and Heckler, G. W., "A GPS Receiver for High-Altitude Satellite Navigation," *IEEE Journal of Selected Topics in Signal Processing*, vol. 3, August 2009.

[7] Jorgensen, P., "Autonomous Navigation of Geosynchronous Satellites Using the NAVSTAR Global Positioning System," in *National Telesystems Conference, Galveston, TX*, 1982.

[8] Wu, S. C., Yunck, T. P., Lichten, S. M., Haines, B. J., and Malla, R. P., "GPS Based Precise Tracking of Earth Satellites from Very Low to Geosynchronous Orbits," in *National Telesystems Conference*, 1992.

[9] Moreau, M. C., *GPS Receiver Architecture for Autonomous Navigation in High Earth Orbits*. PhD thesis, University of Colorado, 2001.

[10] Moreau, M. C., Axelrad, P., Garrison, J. L., and Long, A., "GPS Receiver Architecture and Expected Performance for Autonomous Navigation in High Earth Orbits," *Navigation*, vol. 47, no. 3, pp. 190–204, 2000.

[11] Powell, T., Martzen, P. D., Sedlacek, S., Chao, C., Silva, R., Brown, A., and Belle, G., "GPS Signals in a Geosynchronous Transfer Orbit: Falcon Gold Data Processing," in *Proceedings of the Institute of Navigation National Technical Meeting*, pp. 575–585, January 1999.

[12] Balbach, O., Eissfeller, B., Hein, G. W., Zink, T., Enderle, W., Schmidhuber, M., and Lemke, N., "Tracking GPS Above GPS Satellite Altitude: First Results of the GPS Experiment on the HEO Mission Equator-S," in *Proceedings of IEEE PLANS*, pp. 243–249, 1998.

[13] Moreau, M., Davis, E., Carpenter, R., Davis, G., Jackson, L., and Axelrad, P., "Results from the GPS Flight Experiment on the High Earth Orbit AMSAT AO-40 Spacecraft," in *Proceedings of the ION GPS 2002 Conference, Portland, OR*, 2002.

[14] Kronman, J., "Experience Using GPS For Orbit Determination of a Geosynchronous Satellite," in *Proceedings of the Institute of Navigation GPS*, (Salt Lake City, UT), September 2000.

[15] Spilker, J. J., "GPS Signal Structure and Theoretical Performance," in *Global Positioning System: Theory and Applications*, vol. 1, ch. 3, Progress in Astronautics and Aeronautics, 1997.

[16] Czopek, F. M. and Shollenberger, L. S., "Description and Performance of the GPS Block I and II L-Band Antenna and Link Budget," in *Proceedings of the International Technical Meeting of the ION Satellite Division*, ION GPS, September 1993.

[17] Neumann, N., "In-Flight Results from the GPS Receiver on SmallGEO," in *68th International Astronautical Congress*, (Adelaide, Australia), September 2017.

[18] Barker, L. and Frey, C., "GPS at GEO: A First Look at GPS from SBIRS GEO1," in *Proceedings of the AAS Guidance Navigation and Control Conference*, (Breckenridge, CO), February 2014.

[19] Parker, J. J. K., Donaldson, J. E., Bauer, F. H., and Moreau, M. C., "Use and Protection of the GPS Side Lobe Signals for Enhanced Navigation Performance in High Earth Orbit," in *Ameri-*

can Astronautical Society Guidance, Navigation, and Control Conferece, Breckenridge, CO, AAS, February 2016.

[20] Unwin, M., Van Steenwijk, R. D., Blunt, P., Hashida, Y., Kowaltschek, S., and Nowak, L., "Navigating above the gps constellation – preliminary results from the sgr-geo on giove-a," in *Proceedings of the 26th International Technical Meeting of The Satellite Division of the Institute of Navigation (ION GNSS+ 2013)*, pp. 3305–3315, 2013.

[21] Verde, G., Unwin, M., Duncan, S., Hyslop, A., and Kowaltschek, S., "Revisiting the SGR-GEO on GIOVE-A for GPS Satellite Antenna Pattern Mapping," in *GNC 2017: 10th International ESA Conference on Guidance, Navigation, and Control Systems, Salzburg, Austria*, 2017.

[22] DiOrio, N. A. and Axelrad, P., "GPS Weak Signal Detection for Orbit Determination at Geosynchronous Altitudes." Discovery Learning Student Project Poster at CU-Boulder, April 2012.

[23] Jackson, J. D., *Classical Electrodynamics*. John Wiley and Sons, Inc., 1962.

[24] Crochiere, R. and Rabiner, L., *Multirate Digital Signal Processing*. Prentice-Hall Signal Processing Series: Advanced monographs, Prentice-Hall, 1983.

[25] Stein, S., "Algorithms for Ambiguity Function Processing," *IEEE Transactions on Acoustics, Speech, and Signal Processing*, vol. ASSP-29, June 1981.

[26] Psiaki, M. L., "Block Acquisition of Weak GPS Signals in a Software Receiver," in *Proceedings of the International Technical Meeting of the ION Satellite Division*, ION GNSS, September 2001.

[27] Tsui, J. B. Y., *Fundamentals of Global Positioning Systems Receivers, A Software Approach*. J. Wiley and Sons, New York, 2000.

[28] CGSIC, "Limited Duration GPS C/A Power Testing." `https://content.govdelivery.com/accounts/USDHSCG/bulletins/182c419`, 2017.

[29] NASA Goddard Space Flight Center, "Orbit Determination Toolbox (ODTBX)." `http://sourceforge.net/projects/odtbx/`, 2015.

[30] Bar-Sever, Y. E., "A New Model for Yaw Attitude of Global Positioning System Satellites," *The Telecommunications and Data Acquisition Progress Report 42-123*, November 1995. Available at http://tda.jpl.nasa.gov/progress_report.

[31] "Radio Noise, Recommendation ITU-R P.372-13." `http://www.itu.int/rec/R-REC-P.372-13-201609-I/en`, 2016. International Telecommunications Union.

[32] Dierendonck, A. J. V., "GPS Receivers," in *Global Positioning System: Theory and Applications* (Parkinson, B. and Spilker, J., eds.), vol. 163 of *Progress in Astronautics and Aeronautics*, ch. 8, Washington, DC: AIAA, 1996.

[33] Jones, E., Oliphant, T., Peterson, P., *et al.*, "SciPy: Open source scientific tools for Python, v. 0.7.2." `http://www.scipy.org/`, 2001-2010.

[34] "GPS Antenna Characterization Experiment (ACE) Data." `https://esc.gsfc.nasa.gov/GPS_ACE`, 2019. NASA Goddard Space Flight Center.

[35] Winternitz, L., Bamford, W., Long, A., and Hassouneh, M., "GPS Based Autonomous Navigation Study for the Lunar Gateway," in *Proceedings of the 42nd AAS Guidance and Control Conference (AAS GNC 2019)*, (Breckenridge, CO), February 2019.

[36] Wanninger, L., Sumaya, H., and Beer, S., "Group Delay variations of GPS transmitting and receiving antennas," *J Geod*, vol. 91, pp. 1099–1116, 2017.

[37] Schmid, R., Dach, R., Collilieux, X., Jaggi, A., Schmitz, M., and Dilssner, F., "Absolute IGS antenna phase center model igs08.atx: status and potential improvements," *J Geod*, vol. 90, pp. 343–364, 2016.

[38] Lake, J. and Stansell, T., "SVN-49 Signal Anomaly," in *49th meeting of the Civil GPS Service Interface Committee (CGSIC)*, (Savanna, GA), September 2009. `https://www.gps.gov/cgsic//meetings/2009/stansell.pdf`.

[39] Dybdal, R. B., "GPS Satellite Pseudorange Deviation Contributions," Aerospace Report No. TOR-2014-02719, The Aerospace Corporation, 2014.

[40] Brumbaugh, C., Love, A., Randall, G., Waineo, D., and Wong, S., "Shaped Beam Antenna for the Global Positioning Satellites," in *IEEE AP-S Symposium Digest*, (Amherst, MA), October 1976.

[41] Ashman, B. W., Parker, J. J. K., Bauer, F. H., and Esswein, M., "Exploring the Limits of High Altitude GPS for Lunar Missions," in *American Astronautical Society Guidance, Navigation, and Control Conferece, Breckenridge, CO*, AAS, February 2018.